

Analysis of wave converging phenomena inside the shocked two-dimensional cylindrical water column

Sheng Xu¹, Wenqi Fan¹, Wangxia Wu², Haocheng Wen¹ and Bing Wang^{1,†}

¹School of Aerospace Engineering, Tsinghua University, Beijing 100084, PR China

²School of Aerospace Engineering, Beijing Institute of Technology, Beijing 100081, PR China

(Received 23 July 2022; revised 11 February 2023; accepted 14 March 2023)

Due to the curvature of the droplet surface, the propagation of transmitted waves is complex inside a droplet impacted by an incident shock wave. The wave converging phenomena inside a two-dimensional water column impacted by different curved shock waves are explored in this paper by means of theoretical ray analysis and high-resolution numerical simulations. An analytical method describing the wave structure evolution characteristics inside the shocked water column is established. Hence, the morphological pattern and focus locations of these waves are theoretically obtained. The analysis shows that both the first and the second reflected waves focus inside the water column regardless of the convergent, planar or divergent nature of the incident shock wave shape. The dimensionless distances from focusing points to the column centre are derived as $\kappa/(3\kappa - M_0 f_s)$ for the former and $\kappa/(5\kappa - M_0 f_s)$ for the latter, respectively. Here, κ , M_0 and f_s represent the sound-speed ratio of the two phases, the incident shock wave strength and a function characterising the shock wave shape effect, respectively. Moreover, highly negative pressures due to the first reflected wave focusing and significant pressure oscillations due to the second reflected wave focusing are numerically tracked for three shapes of the incident shock. The effects of the incident shock wave intensity on the pressure variations at focus points are further studied. As the incident shock wave intensity increases, stronger negative pressure and higher pressure oscillation are induced. The converged incident shock wave can enhance the above phenomena, but the diverged one can weaken them.

Key words: shock waves, drops, gas/liquid flow

† Email address for correspondence: wbing@mail.tsinghua.edu.cn

1. Introduction

The phenomenon of a droplet impacted by shock waves occurs widely in natural and industrial scenarios such as two-phase supersonic combustors (Malik *et al.* 2022), supernova explosions (Abgrall & Karni 2001), cavitation (Brennen 2013) and shock wave lithotripsy (Johnsen & Colonius 2009). In the development of hypersonic propulsion systems, in particular, it is of great interest to understand the behaviours of fuel droplets interacting with shock waves. In previous studies, this thread of investigations has mainly been presented in regard to three aspects, which are: the deformation mechanism of the shocked droplet, the wave evolution characteristics and the cavitation behaviours inside the shocked droplet.

Over the past decades, continuous efforts to reveal the deformation and breakup mechanism of the shocked droplet or liquid column have been made via theoretical analyses, experimental investigations and numerical simulations. As a classical result, the breakup modes of droplets, without the impacts of the shock wave, are classified into five regimes denoted as vibrational, bag, bag and stamen, stripping and catastrophic breakup, which are described in the works of Pilch & Erdman (1987) and Hsiang & Faeth (1992, 1993). Furthermore, Theofanous, Li & Dinh (2004) and Theofanous & Li (2008) reclassified the breakup modes into two regimes with consideration of the effect of incident shock wave impaction, namely the Rayleigh–Taylor piercing mode and shear-induced entrainment mode. Meng & Colonius (2015) numerically studied the interaction of a planar shock wave with a water column and described the deformation characteristics of the water column under different shock wave intensities. Then, Meng & Colonius (2018) studied the interaction between a planar shock and a spherical droplet, hence analysing the droplet deformation characteristics. Through high-magnification and high-speed breakup images, Biasiori-Poulanges & El-Rabii (2019) demonstrated the evolution dynamics of the breakup process at a higher Weber number. Sharma *et al.* (2021) detailly investigated the initial wave dynamics and droplet breakup dynamics of the interaction dynamics between a liquid droplet and a planar shock wave in a wide range of Weber numbers and Reynolds numbers.

In this area of study, the evolution characteristics of waves inside a droplet are still a subject that is under studied. Igra & Takayama (2001*a,b*), Igra & Sun (2010) and Meng & Colonius (2015) showed that early stages of shock wave propagation events inside the liquid droplet are an inherent part of the aero-breakup problem. In addition, Igra & Sun (2010) pointed out that the two-dimensional cylindrical water column behaves similarly to a spherical droplet when comparing droplet deformation and disintegration. However, considering the transient time scale, visualising the complex wave structures propagating inside the spherical droplet presents a huge challenge in experimental studies. Numerous studies have been the primary choice in investigating the flow characteristics inside a liquid column. Sembian *et al.* (2016) detailly reported the wave structure evolution at the early stages of planar shock wave interaction with a cylindrical water column under different incident shock wave intensities. The work revealed the evolution characteristics of the wave structures inside the liquid column impinged by a planar shock wave. Boyd & Jarrabashi (2021) extended the shock–droplet interaction problem from the subcritical condition to the supercritical condition and studied the effects of temperature, pressure and shock intensity on the interaction. Based on the ray analysis method (Heymann 1969; Haller *et al.* 2003; Wu, Xiang & Wang 2018), Biasiori-Poulanges & El-Rabii (2021) theoretically investigated the interaction of a planar shock wave with a liquid column and derived the concentration of rays with different reflection times and then verified their results by numerical simulations. Guan *et al.* (2018) numerically and theoretically investigated

the establishment of an internal flow field inside a water droplet subjected to shock wave impact. In their work, a saddle point inside the water droplet is observed for the first time, chosen as a characteristic point to describe the internal flow.

In the current literature, it has been stated that the propagating expansion waves inside the droplet can induce a cavitation phenomenon. However, the criteria are yet to be established since the process is highly transient. The possibility of cavitation in the water column due to the expansion wave focusing at higher shock Mach numbers was observed in the works of Sembian *et al.* (2016). Field, Dear & Ogren (1989) and Field *et al.* (2012) observed that, when a high-speed droplet impacts a rigid wall, convergence of reflected expansion waves could cause cavitation bubbles. The possibility of cavitation of a high-speed droplet impacting the wall was verified by Kondo & Ando (2016), Wu *et al.* (2018) and Wu, Liu & Wang (2021*b*) via the numerical method. Xiang & Wang (2017) and Biasiori-Poulanges & El-Rabii (2021) expounded that the occurrence of cavitation inside the shocked water column is dependent on the incident shock wave intensity and the value of the cavitation threshold pressure. Moreover, Xiang & Wang (2017) performed a numerical study on the interaction of a planar shock wave with a water column embedded with air cavities of different sizes at high Weber numbers. Liang *et al.* (2020) captured the deformation of a water droplet embedded within a vapour cavity and analysed the influence of the relative size and eccentricity of the vapour cavity on the mechanism of droplet deformation. The results show that the embedded cavity inside the water column or droplet can significantly affect the deformation characteristics.

Summarising the past decades, the planar shock wave interacting with a liquid droplet/column has been widely studied, and the droplet deformation and the inherent evolution characteristics of wave structures have been well investigated experimentally, numerically and theoretically. However, in some practical application scenarios, such as the ultrasound-assisted treatment of human tissues (Feril & Kondo 2004; Kim *et al.* 2008; Lukka *et al.* 2010), it is quite hard for the wavefront to achieve an ideal plane (Sembian *et al.* 2016). Moreover, Mittelstein *et al.* (2020) and Landgraf *et al.* (2022) reported that, in obtaining the desirable cavitation phenomena, e.g. the micro-bubble cavitation process as being an enhancer of bioeffects reported by Feril & Kondo (2004), the regulation of the location of the focus point and the negative pressure intensity near the focus point are critical. For this reason, the utilisation of the cavitation effect is subject to a certain deviation when only the influence of the planar shock wave intensity is considered. In addition, even when an ideal planar shock wave would be achieved by more advanced technologies, simultaneously achieving precise regulation of the focus point position and the negative-pressure intensity by adjusting the intensity of the incident wave remains a challenge. In this context, it is of interest to reveal the effects of the incident shock wave shape on the focus point location and negative pressure intensity. Therefore, through theoretical analysis and numerical simulations, this study aims to investigate the wave converging phenomena inside a two-dimensional water column impinged by a curved shock wave. The findings concluded in this study are expected to help researchers attain the migration of the focus point and amplify or reduce the negative-pressure intensity near the focus point through suitable wavefront shape designs and the adjustment of the incident shock wave intensity.

This paper is organised as follows. In § 2, the physical model of the interaction between the curved shock wave and a water column is described, and the theoretical tool of the ray analysis method is established, and the governing equations, numerical treatments and numerical validation are presented. In § 3, the morphology and dynamical evolutions of wave structures are analysed qualitatively and quantitatively, taking the interaction of a

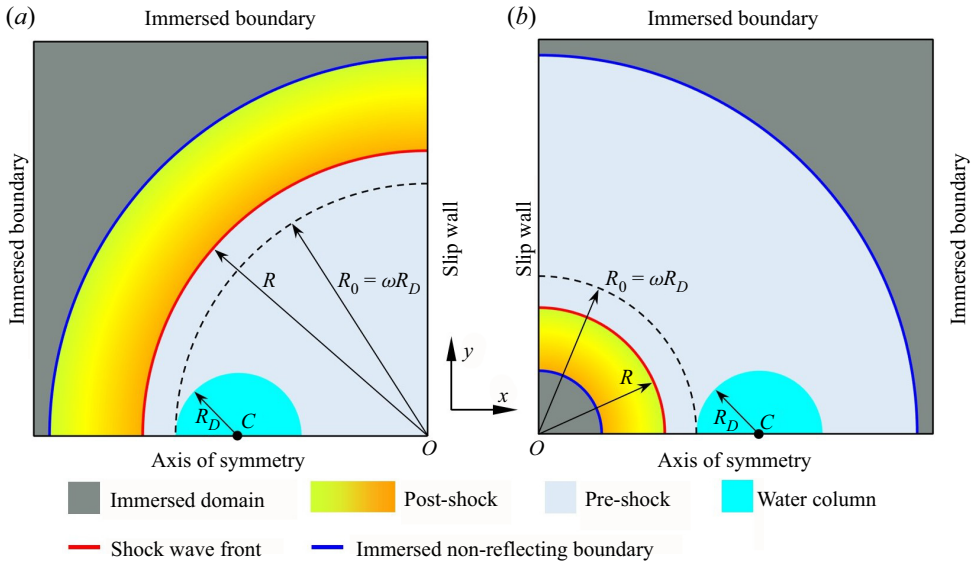


Figure 1. Schematic diagram of the interaction of a cylindrical shock with a water column. (a) The interaction of a converged shock with a water column; (b) the interaction of a diverged shock with a water column.

cylindrical converged shock wave with a water column as an example. In § 4, the effects of intensities and shapes of the incident shock wave are investigated. Finally, the conclusions are presented in § 5.

2. Physical model and numerical procedure

2.1. Physical model

The previous study (Igra & Sun 2010) has shown that the flow characteristics inside the two-dimensional water column are similar to those inside the spherical droplet, and that three-dimensional numerical simulation comes at a huge CPU time cost. Hence, the two-dimensional water column is chosen in the present study to save computing resources as much as possible and improve computing efficiency. A schematic diagram of the interaction of a cylindrical incident shock wave with a water column is shown in figure 1, including a converged and diverged one. We use R_0 to represent the radius of the cylindrical shock wave when it just touches the water column and R_D to represent the radius of the water column. Moreover, the dimensionless radius $\omega (= R_0/R_D)$ is used to normalise the curvature effect of the incident shock wave. Referring to the experiment (Igra & Takayama 2001a) and numerical simulation (Xiang & Wang 2017), the initial value of R_D is taken as 2.4 mm. Moreover, we use C and O to represent the water column centre and the origin of coordinates, respectively. The water column and the air ahead of the shock wave are initially in equilibrium with a temperature of 300 K and a pressure of 101 325 Pa. The Weber numbers in the present numerical simulations are higher than 1000, and the corresponding Reynolds numbers are over 40 000. Therefore, the viscosity and the surface tension can be neglected in the present study (Meng & Colonius 2015).

In the present study, the generation of the cylindrical shock wave is based on the theory of shock dynamics, which can characterise the propagation of shock waves with an arbitrary profile. The Chester–Chisnell–Whitham (CCW) relation is the basis of shock

Curved shock interaction with water column

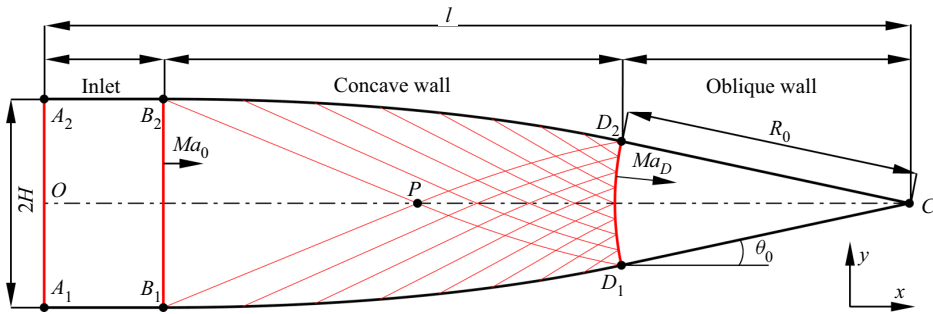


Figure 2. The schematic drawing of the wall profile, transforming the planar shock into a cylindrical one. Here, H is the half-height of the V-shaped geometry; l the length of the V-shaped geometry; Ma_0 the Mach number of the incident planar shock waves; Ma_D the Mach number of the cylindrical shock wave; θ_0 the half-converging angle.

dynamics for a uniform quiescent gas ahead of shock, which is referred from Chester (1954), Chisnell (1957) and Whitham (1957, 1958, 1959). The CCW relation describes how the shock wave Mach number M varies with the shock-front area A ($= 2\pi R$ in two-dimensional cases), which can be written as

$$\frac{2M \, dM}{(M^2 - 1)K(M)} + \frac{dA}{A} = 0, \quad (2.1)$$

where

$$K(M) = 2 \left[2\mu + 1 + \frac{1}{M^2} \right]^{-1} \left[1 + \frac{2}{\gamma + 1} \left(\frac{1}{\mu} - \mu \right) \right]^{-1}, \quad \mu = \sqrt{\frac{(\gamma - 1)M^2 + 2}{2\gamma M^2 - (\gamma - 1)}}. \quad (2.2)$$

Zhai *et al.* (2010) used this shock dynamics theory to design a curved wall profile (V-shaped geometry) and realised the transformation from a planar shock wave to a cylindrical converged shock wave, as shown in figure 2. Both numerical and experimental results show a perfect circular shock front. However, this method comes at enormous computing resource cost due to the large computation domain and usually can only obtain a cylindrical shock wave with a small converging angle ($= 2\theta_0$), which leads to a small range of radius of the water column that can be investigated in the present study. Hence, a 90° computational domain is used in this paper, as shown in figure 1(a), which is widely used in the literature (Lombardini, Pullin & Meiron 2014; Zhai *et al.* 2019; Wu, Liu & Xiao 2021a). The fluid variables behind the cylindrical shock wave are calculated by the following algorithm: given the cylindrical shock radius of R_0 , the cylindrical shock wave intensity M_0 and fluid variables ahead of the incident cylindrical shock wave p_0 and T_0 . When the radius of the cylindrical shock wave is R , the intensity of the cylindrical shock wave M satisfies

$$\int_{M_0}^M \frac{2m \, dm}{(m^2 - 1)K(m)} = - \int_{R_0}^R \frac{dr}{r}. \quad (2.3)$$

Integrating (2.3) by numerical iteration, the value of M is obtained. Further, using the Rankine–Hugoniot conditions, the fluid variables behind the cylindrical shock wave can be calculated, including pressure p , density ρ , temperature T and velocity magnitude V_m . The accuracy verification of CCW theory is presented in detail in Appendix A.

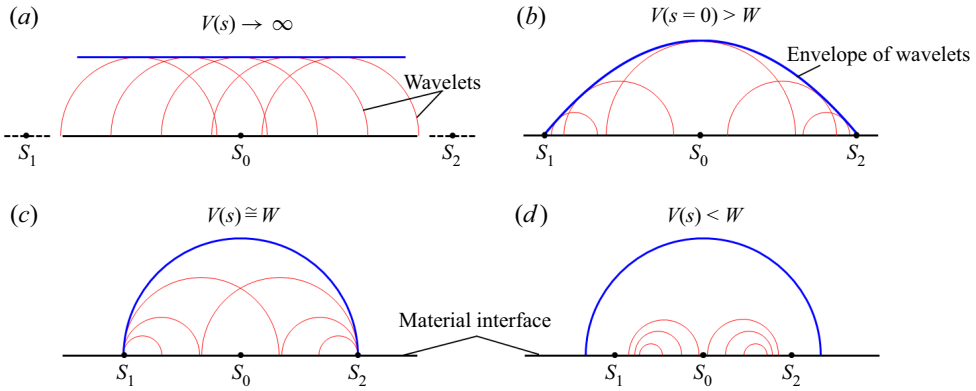


Figure 3. Schematic diagram of the Huygens principle.

2.2. Method of the ray analysis

In this sub-section, the ray analysis method (Heymann 1969; Haller *et al.* 2003; Wu *et al.* 2018), which is based on the Huygens principle used in the theoretical analysis of wave configurations, is presented. For convenience, two moving point disturbances, which are denoted as S_1 and S_2 , and a straight material interface are used to briefly introduce the ray analysis method, as shown in figure 3. At the initial instant, two moving point disturbances coincide at point S_0 , located on the straight interface. Then these two point disturbances move away from S_0 in opposite directions with the same speed, which gradually decreases with distance s from S_1 (S_2) to S_0 and is denoted as $V(s)$. Based on the Huygens principle, an individual wavelet will be emitted at each instant at $S_1(s)$ and these individual wavelets propagate at a constant speed of W . It can be seen that the envelope of all individual wavelets generated before t forms the wavefront induced by these two moving point disturbances. According to the relationship between $V(s)$ and W , there are four envelope shapes, as shown in figure 3(a–d). Note that, for the case corresponding to figure 3(b), when the propagation speed of the point disturbance $V(s)$ is less than W , the newer individual wavelets cannot catch up with the envelope of wavelets, as will be explained in detail in § 3.1.

For three cases except for the case corresponding to figure 3(b), it is not difficult to understand the position and shape of the envelope of wavelets, while it is still confusing to understand the evolution characteristics of the envelope for the rest of the cases. Hence, the ray analysis method is used, as shown in figure 4. The propagation of each wavelet can be equivalent to the propagation of infinite rays emitted at its origin, and the length of the ray is equal to the propagation distance of the wavelet. It is obviously found that not all of the rays emitted from the same wavelet can effectively contribute to the envelope of wavelets. Therefore, to reveal the physical mechanism of the motion of the wavefront induced by point disturbances, it is necessary to find these special rays which have contributed to the envelope of wavelets. Here, the two wavelets emitted from S_s and $S_{s+\Delta s}$ are selected for detailed discussion, as shown in figure 4(b), and these two emission points are very close to each other. The radii of these two wavelets are $r(t, s)$ and $r(t, s + \Delta s)$, respectively,

$$r(t, s) = W(t - t_s), \quad r(t, s + \Delta s) = W(t - t_{s+\Delta s}), \quad (2.4)$$

where t_s represents the time for moving point disturbance S_1 from S_0 to $S_1(s)$.

The intersection point of these two wavelets is G_s , and the angle between the vector $\overrightarrow{S_s S_{s+\Delta s}}$ and $\overrightarrow{S_s G_s}$ is α_s , as shown in figure 4(b). The expression α_s is derived from the law

Curved shock interaction with water column

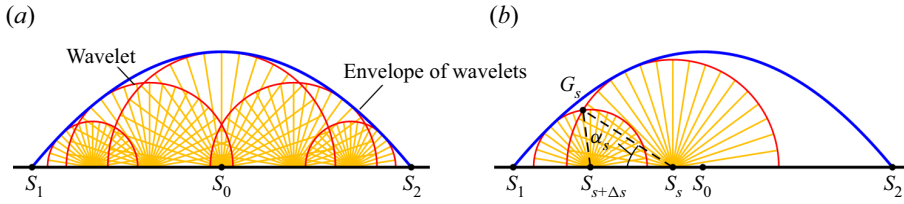


Figure 4. Schematic diagram of the ray analysis method.

of cosines in the triangle $\Delta S_s S_{s+\Delta s} G_s$

$$\cos \alpha_s = \frac{(2t - t_s - t_{s+\Delta s}) (t_{s+\Delta s} - t_s) W}{2(t - t_s)} + \frac{\Delta s}{2(t - t_s) W}. \quad (2.5)$$

When $S_{s+\Delta s}$ is infinitely close to S_s ($\Delta s \rightarrow 0^+$), α_s is the angle between the vector of the emitted ray and the material interface. The endpoint of this ray is the unique contribution of the wavelet emitted from S_s to the envelope of wavelets

$$\begin{aligned} \cos \alpha_s &= \lim_{\Delta s \rightarrow 0^+} \left[\frac{(2t - t_s - t_{s+\Delta s}) (t_{s+\Delta s} - t_s) W}{2(t - t_s)} + \frac{\Delta s}{2(t - t_s) W} \right] \\ &= \lim_{\Delta s \rightarrow 0^+} \frac{(t_{s+\Delta s} - t_s) W}{\Delta s} = W t'_s. \end{aligned} \quad (2.6)$$

Equation (2.6) shows that the emission angle of these particular rays is only determined by the propagation speed of the wavelets and the kinematic characteristics of the moving point disturbance along the material interface. Note that, if the material interface were a closed curve, these rays would reflect on the material interface after a period of propagation. This reflection property will be investigated in detail in § 3.1.

2.3. Numerical models

The interaction between the shock wave and the droplet is a strong compressible multiphase hydrodynamics problem, which involves complex factors such as a large density ratio and strong shock waves. In this paper, the numerical simulation is carried out by the in-house software (SCP-tran[®]), which was previously applied to study a variety of compressible multiphase flow problems (Xiang & Wang 2017; Wang, Xiang & Hu 2018; Wu *et al.* 2018). The five-equation model (Allaire, Clerc & Samuel 2002; Johnsen & Colonius 2006) is used to solve the gas–liquid hydrodynamic system, and the governing equations consist of two continuity equations for each phase, a mixture momentum equation, a mixture energy equation and a volume fraction advection equation

of the liquid phase

$$\left. \begin{aligned} \frac{\partial(\alpha_l \rho_l)}{\partial t} + \frac{\partial(\alpha_l \rho_l u)}{\partial x} + \frac{\partial(\alpha_l \rho_l v)}{\partial y} &= 0, \\ \frac{\partial(\alpha_g \rho_g)}{\partial t} + \frac{\partial(\alpha_g \rho_g u)}{\partial x} + \frac{\partial(\alpha_g \rho_g v)}{\partial y} &= 0, \\ \frac{\partial(\rho u)}{\partial t} + \frac{\partial(\rho u^2 + p)}{\partial x} + \frac{\partial(\rho uv)}{\partial y} &= 0, \\ \frac{\partial(\rho v)}{\partial t} + \frac{\partial(\rho uv)}{\partial x} + \frac{\partial(\rho v^2 + p)}{\partial y} &= 0, \\ \frac{\partial \rho E}{\partial t} + \frac{\partial[(\rho E + p)u]}{\partial x} + \frac{\partial[(\rho E + p)v]}{\partial y} &= 0, \\ \frac{\partial \alpha_l}{\partial t} + u \frac{\partial \alpha_l}{\partial x} + v \frac{\partial \alpha_l}{\partial y} &= 0, \end{aligned} \right\} \quad (2.7)$$

where ρ_l and ρ_g represent the density of the liquid and gas phases, respectively, α_l and α_g represent the volume fraction of the liquid and gas phases, respectively, ρ , u , v , p and E represent the mixture density, x -velocity, y -velocity, pressure and specific total energy, respectively. The numerical diffusion appears significant at the two-phase interface after several time steps. In this diffuse region, the mixture variables are given as (Saurel, Petitpas & Abgrall 2008)

$$\rho = \alpha_l \rho_l + \alpha_g \rho_g, \quad (2.8)$$

$$\rho E = \alpha_l \rho_l e_l + \alpha_g \rho_g e_g + \frac{1}{2} \rho (u^2 + v^2), \quad (2.9)$$

$$\rho c^2 = \alpha_l \rho_l c_l^2 + \alpha_g \rho_g c_g^2, \quad (2.10)$$

where e_l and e_g represent the specific internal energy of the liquid and gas phases, respectively, c_l and c_g represent the sound speed of the liquid and gas phases, respectively. In this study, the stiffened gas equation of state is used to close the governing equations

$$\rho_k e_k = \frac{p + \gamma_k p_{\infty, k}}{\gamma_k - 1}, \quad k = l, g, \quad (2.11)$$

$$c_k = \sqrt{\frac{(p + p_{\infty, k}) \gamma_k}{\rho_k}}, \quad k = l, g, \quad (2.12)$$

where γ is the specific heat ratio and p_{∞} is the reference pressure. For air, $\gamma = 1.4$ and $p_{\infty} = 0$, and the stiffened gas equation of state reduces to the ideal gas equation. Referring to the works of Kondo & Ando (2016) and Xiang & Wang (2017), the parameters for water are taken to be $\gamma = 6.12$ and $p_{\infty} = 343.44$ MPa.

2.4. Numerical treatments

The SCP-tran[®] fluid dynamic software uses a finite volume method (Titarev & Toro 2004) to discretise the above governing equations in a uniform Cartesian grid system. The component-wise fifth-order incremental weighted essentially non-oscillatory reconstruction is applied, as previously proposed by the present author (Wang *et al.* 2018).

The Harten–Lax–van Leer contact approximate Riemann solver (Toro 2009) is employed to solve the numerical flux at the cell face. The third-order total variation diminishing Runge–Kutta method (Gottlieb & Shu 1998) is chosen to advance the solutions over time. Considering that part of the boundaries does not coincide with the interface of the grid cell, such as the immersed non-reflecting boundary as shown in figure 1, a ghost-cell immersed boundary method (IBM) for distinguishing geometrically complex boundaries is used to realise the non-reflecting boundary condition (Thompson 1987, 1990), and for the detail of IBM the reader is referred to the works of Choung *et al.* (2021) and Saravanan, Choung & Lee (2021). Since the evolution characteristics of the interaction between shock waves and the water column are symmetric, to improve the calculation efficiency, the symmetric boundary condition at the axis of the liquid column is adapted to carry out numerical simulations. The numerical verification of the grid sensitivity is presented in Appendix B.

2.5. Validation of the solver

Thanks to the experiments in the literature, the interaction of a planar shock wave with a water column is chosen as a validation case to validate the SCP-tran[©] fluid dynamic software. For a qualitative comparison, the dimensionless time t^* is used, which is the ratio of the physical time over the characteristic time τ ($\tau = 2R_D/V_{ts}$, V_{ts} is the propagation speed of the transmitted shock wave). For convenience, the zero instant is marked as t_0 ($t^* = 0.0$) when the incident shock wave just touches the water column. According to the Rankine–Hugoniot relation (Haller *et al.* 2002, 2003; Nagayama *et al.* 2006), the transmitted shock wave speed V_{ts} can be estimated as

$$V_{ts} = \frac{\gamma_l + 1}{4} \left(u_l + \sqrt{u_l^2 + 16 \frac{1}{(\gamma_l + 1)^2} c_{l,0}^2} \right), \quad (2.13)$$

where γ_l represents the specific heat ratio of water, $c_{l,0}$ ($\sim 1500.0 \text{ m s}^{-1}$) represents the sound speed of the water at the initial state (300 K and 101 325 Pa) and u_l represents the velocity of the liquid inside the water column behind the transmitted shock wave. Due to the acoustic impedance of water being much higher than that of air, most of the energy of the incident shock wave is reflected. Hence, the velocity change of the water is almost zero, no bigger than 5.0 m s^{-1} , before and after the impingement of the incident shock wave, and the sound speed of water $c_{l,0}$ can be chosen as an equivalent of V_{ts} .

Figure 5 shows the comparisons between the numerical result based on the present numerical methods and the experimental results from Sembian *et al.* (2016) of the interaction of a planar shock wave with a water column for $M_0 = 2.4$. When the planar incident shock wave impinges on the water column, it is reflected off the column surface and transmitted into the water column. As the interaction continues, the Mach stem and the slip line appear subsequently. Due to the specific water column surface, the reflected rarefaction wave (Sembian *et al.* 2016) (also called the reflected expansion wave) will focus inside the water column. These flow structures have been observed both in experiments and simulations. Besides the qualitative analysis, the quantitative comparison of the pressure profiles of the two sensors inside the water column between the experimental result and numerical simulations is also presented in figure 6. It is found that our numerical method (SCP-tran[©]) can effectively capture the pressure evolutions inside the water column, and is in good agreement with the numerical result and is also approximately in agreement with the experimental result. Due to the SCP-tran[©] software having higher accuracy of the time advance and the space discretisation causing lower numerical dissipation,

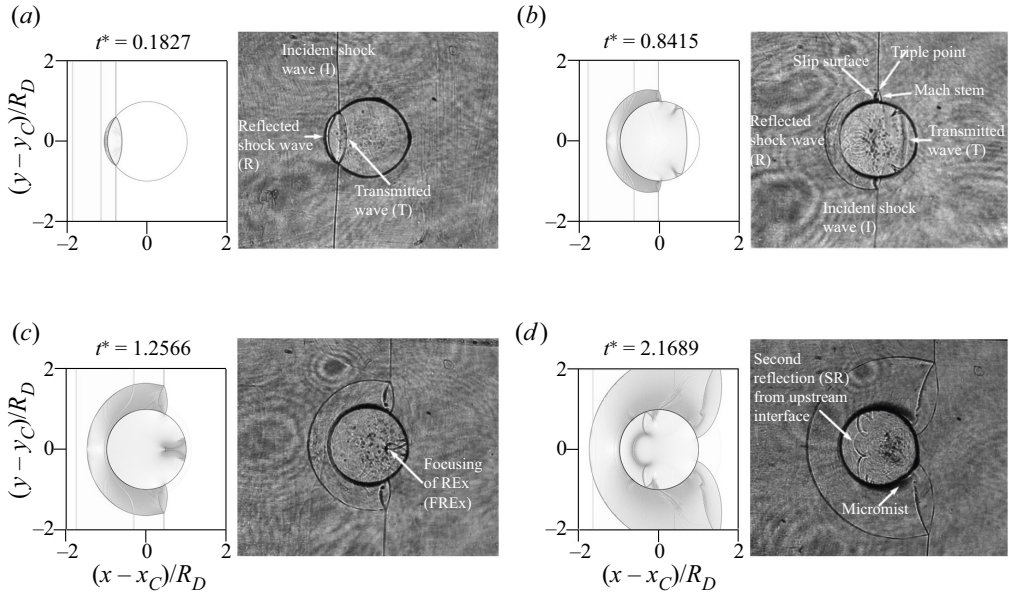


Figure 5. The comparison between the present simulation results (left side) and the experimental results (right side) from Sembian *et al.* (2016) of the interaction of a planar shock wave with a water column for $M_0 = 2.4$.

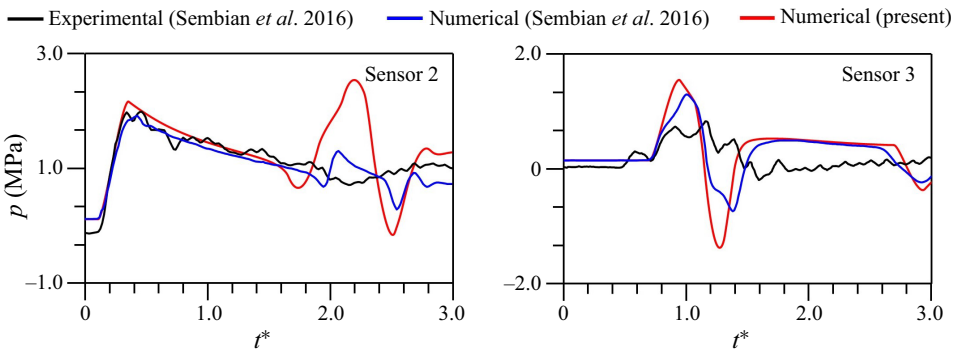


Figure 6. Experimental and numerical pressure profile for $M_0 = 2.4$. The locations of sensors 2 and 3 are given in the work of Sembian *et al.* (2016). Note that the diaphragm diameter of the sensor is 5.54 mm, and therefore the values obtained are averaged across the sensor's face area. Similarly, numerical simulation results are also averaged.

compared with the work of Sembian *et al.* (2016), the present numerical result obtains stronger focus pressures, especially for the focus of the second reflected waves, as shown in figure 6(a). Note that the sensing geometry is compressed; hence, the sensor cannot quantitatively measure the negative pressure in experimental research. Both the qualitative wave configuration analysis and the quantitative pressure profile analysis show that the present mathematical models and numerical methods are able to solve the problem of the interaction of the shock wave with a water column.

It is necessary to illustrate that the planar incident wave, in experiments (Sembian *et al.* 2016), is a blast wave with gradually decreasing strength rather than a shock wave with a uniform post-shock flow. This substitution causes different pressure distributions

inside the water column and then induces different cavitation behaviours. However, the main purpose of the present work is to demonstrate the propagation characteristics of waves inside the water column, which are almost the same between the blast wave with a decreasing post-shock flow and the shock wave with a uniform post-shock flow when the shock intensity is the same. Hence, the planar shock with a constant Mach number is chosen in the present study for simplification as much as possible and to improve computing efficiency. Of course, when it is necessary to deeply understand the evolution characteristics of the cavitation phenomenon inside a water column impacted by a weak shock wave, an analytical solution for blast waves, described by Bach & Lee (1970), can be chosen to generate a stable blast wave without much increase in computational cost.

3. Evolution characteristics of wave structures inside the water column

In this section, the cylindrical converged shock wave is taken as an example to analyse in detail the evolution characteristics of wave structures inside the shocked water column.

Figure 7 shows the numerical results in the early stage of the interaction between a cylindrical converged shock wave and a water column in the case of $\omega = 4.0$ and $M_0 = 2.4$. For the visualisation of the numerical simulations, both numerical schlieren contours and pressure contours are presented. Similar to the planar shock wave/water column interaction (Sembian *et al.* 2016; Xiang & Wang 2017), a transmitted shock wave is generated and propagates inside the water column after the impingement of a cylindrical converged shock, figure 7(b). As the sound speed in the water is much bigger than the propagation speed of the incident shock wave, the transmitted shock wave quickly detaches from the incident shock and the reflected shock wave and forms a precursor transmitted shock wave, figure 7(d). In the air, the reflection transition of the incident converged shock wave from the regular to Mach reflection occurs after a while, figure 7(d). Meanwhile, the transmitted shock wave is reflected by the water column surface as it propagates and a series of rarefaction waves are generated, as shown in figure 7(e). These rarefaction waves tend to focus inside the water column due to the curved column surface, and this causes a rapid decrease of pressure near the first-focus region, figure 7(h). After complete focus, the rarefaction wave propagates toward the left pole of the water column and is reflected by the column surface, generating a series of second reflected waves. Different from the first reflected rarefaction wave, the second reflected wave has two branches with different properties: the second reflected compression wave and the second reflected rarefaction wave, as shown in figure 7(j). These two branches of the second reflected waves focus at the same position inside the water column in a very short time interval, causing a violent pressure oscillation near the second-focus area, as shown in figure 7(k–l). In principle, the N th reflection wave will appear and focus inside the water column, while the strength of wave structures will be significantly weakened as the times of reflection increase. Therefore, the evolution characteristics of wave structures generated by the first two reflections are only investigated in the following content.

To better understand the physical mechanism of wave structures, the early stage of the interaction between a curved shock wave and a water column can be analysed in three stages according to the flow characteristics. The different behaviour of the transmitted waves inside the water column is the main concern for the convenience of division. The first stage is the generation, propagation and reflection of the transmitted shock wave inside the water column, corresponding to figure 7(a–f). The second stage is the propagation and converging phenomena of the first reflected rarefaction wave, corresponding to figure 7(g–j). The third stage is the propagation and converging phenomena of the second reflected waves, corresponding to figure 7(k–l).

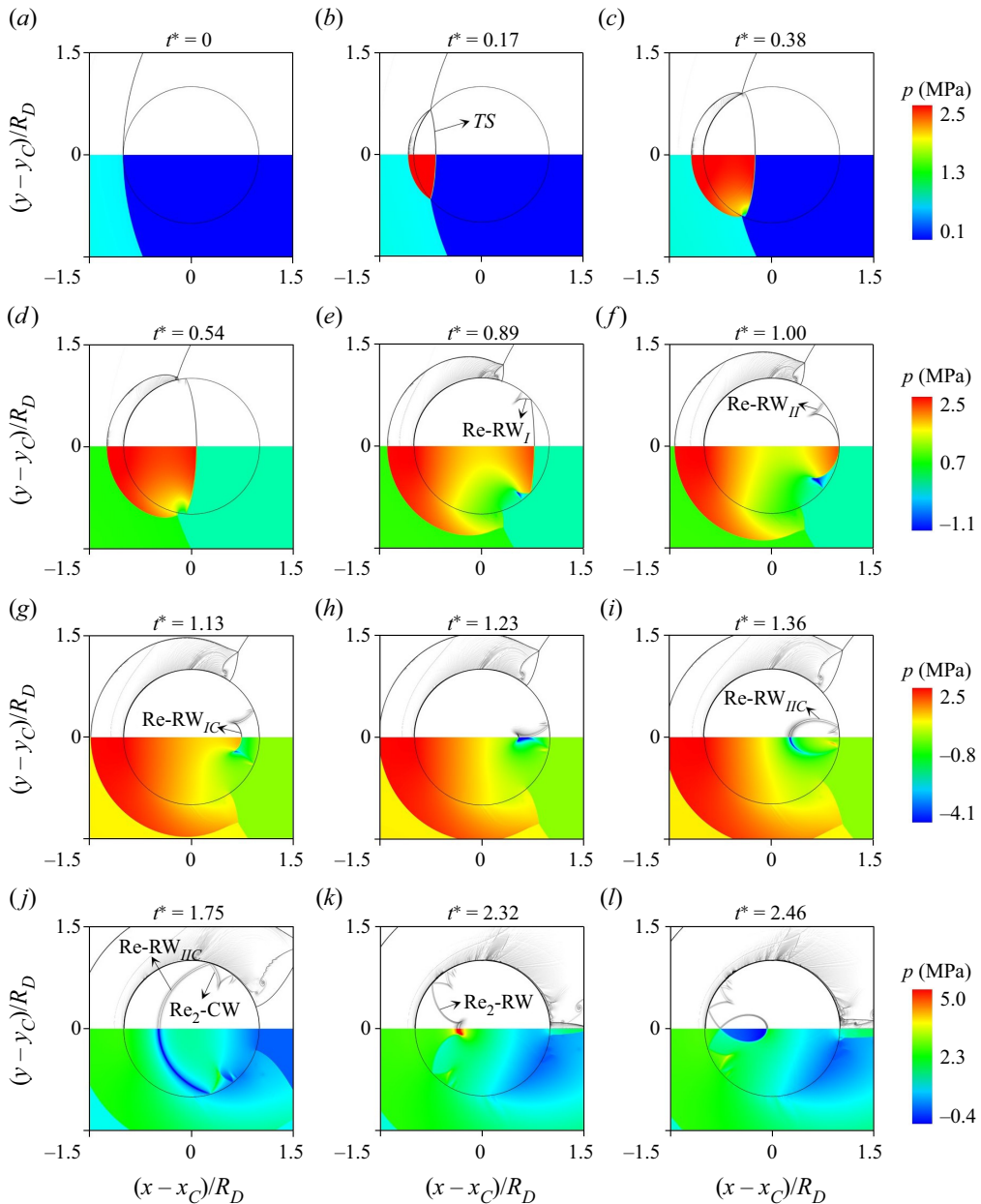


Figure 7. Numerical schlieren contours (top) and pressure contours (bottom) at different time intervals for the interaction between the cylindrical converged shock and the water column in the case of $\omega = 4.0$ and $M_0 = 2.4$. Note that the black line in the pressure contours represents the initial outline of the water column.

3.1. The generation and propagation of the transmitted shock wave

The first stage begins at t_0 ($t^* = 0.0$) when the incident curved shock wave just impacts the left pole of the water column, [figure 7\(a\)](#). During the interaction of a cylindrical converged shock wave with a water column, the contact point is denoted as P_θ , and the angle θ represents the angle between the line $P_\theta C$ and the horizontal axis of the water column, as

Curved shock interaction with water column

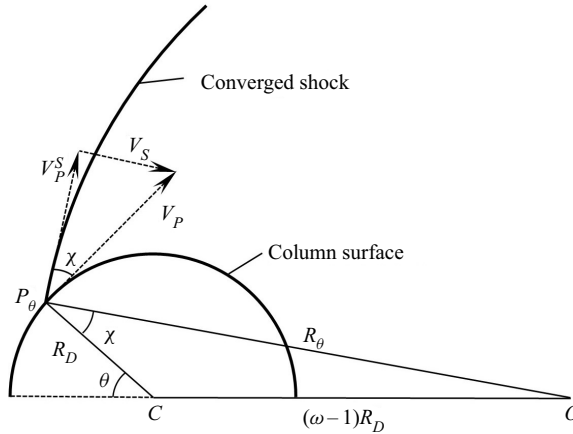


Figure 8. Schematic diagram of the interaction between the cylindrical converged shock wave and the water column.

shown in figure 8. The radius of the cylindrical shock wave is a function of angle θ and is denoted as R_θ . The angle between the tangent line of the water column and that of the converged shock wave is denoted as χ

$$R_\theta = R_D \sqrt{1 + (\omega - 1)^2 + 2(\omega - 1) \cos \theta}, \quad (3.1)$$

$$\sin \chi = \frac{(\omega - 1) \sin \theta}{\sqrt{1 + (\omega - 1)^2 + 2(\omega - 1) \cos \theta}}. \quad (3.2)$$

At a specific contact angle θ , the velocity of contact point P_θ along the water column surface can be expressed by

$$V_P = \frac{V_S}{\sin \chi} = V_S \frac{\sqrt{1 + (\omega - 1)^2 + 2(\omega - 1) \cos \theta}}{(\omega - 1) \sin \theta}, \quad (3.3)$$

where the velocity of the cylindrical converged shock wave V_S is the product of the sound speed of air ahead of the shock front $c_{g,0}$ and the Mach number of the cylindrical shock wave M_θ at P_θ . Because the strength M_0 and the radius R_0 of a cylindrical converged shock wave at t_0 are known, the strength of the cylindrical shock wave at P_θ can be solved from (2.3).

When the contact angle is close to zero, the velocity V_P is much higher than the sound speed of the water, and the transmitted shock wave is attached to the cylindrical incident shock wave and reflected shock wave at the water column surface. Since V_P decreases rapidly as θ increases, as shown in figure 9, the velocity of the contact point on the column surface will catch up with the propagation speed of the transmitted shock wave, and the confined transmitted shock wave will detach from the incident shock wave. The critical time, representing the transmitted shock wave just being detached, is defined as t_{cr} . At the critical time, the velocity of contact point V_P equals the propagation velocity of transmitted wave V_{ts} , and the critical contact angle θ_{cr} satisfies the following expression:

$$\frac{\sqrt{1 + (\omega - 1)^2 + 2(\omega - 1) \cos \theta_{cr}}}{(\omega - 1) \sin \theta_{cr}} = \frac{c_{l,0}}{M_{\theta_{cr}} c_{g,0}}, \quad (3.4)$$

where $M_{\theta_{cr}}$ represents the strength of the incident cylindrical shock wave at t_{cr} . In this section ($\omega = 4.0$ and $M_0 = 2.4$), the value of the critical angle is 44.9° .

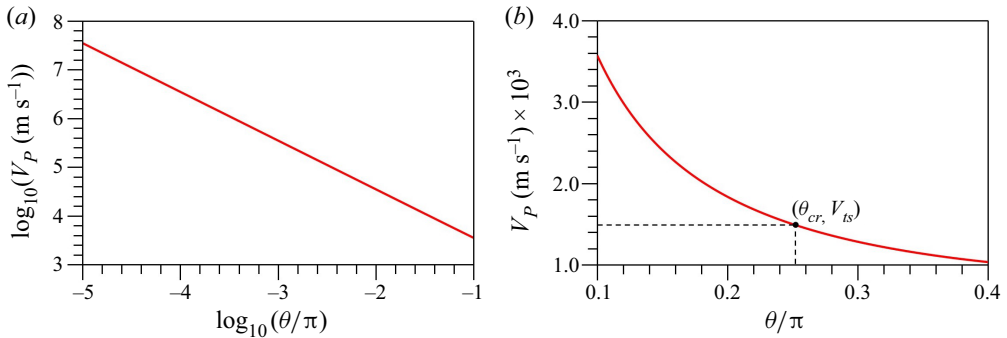


Figure 9. The velocity of the contact point P , along the column surface, varies with the contact angle θ .

Once θ is larger than θ_{cr} , the precursor transmitted shock wave is formed and propagates to the right pole of the water column. The time for contact point to move from the left pole of the water column to P_θ is denoted as t_θ , and its expression can be written as

$$t_\theta = \int_0^\theta \frac{(\omega - 1) \sin \xi R_D}{\sqrt{1 + (\omega - 1)^2 + 2(\omega - 1) \cos \xi M_\xi c_{g,0}}} d\xi. \quad (3.5)$$

Combined with (3.4), the critical instant t_{cr} can be obtained when the transmitted shock wave detaches from the incident shock wave.

Based on the ray analysis method introduced in § 2.2, at each instant, an individual compression wavelet will be emitted at P_θ that will propagate with the water sound speed $c_{l,0}$. Hence, the radius of the compression wavelet emitted from the contact point P_θ , at time instant t , can be denoted as $r(\theta, t) = (t - t_\theta)c_{l,0}$. These compression wavelets, emitted from different contact points from zero instant to time instant t , form a shock wave envelope, denoted as TS_t , figure 10(a). When $t > t_{cr}$, the propagation speed of the compression wavelet is higher than the generation speed of the new compression wavelet, and the new compression wavelet cannot catch up with the transmitted shock wave and does not make an effective contribution to the shock wave envelope, forming the precursor transmitted shock wave, as shown in figure 10(b).

Similar to the discussion in § 2.2, it can be obviously found that not all of the rays emitted from the same compression wavelet make an effective contribution to the shock wave envelope of compression wavelets. Therefore, to reveal the physical mechanism of the motion of the transmitted shock wave, it is necessary to find these special rays which have contributed to the envelope of compression wavelets. Here, the two different compression wavelets emitted from P_θ and $P_{\theta+\Delta\theta}$ are selected for detailed discussion, and these two emission points are infinitely close to each other ($\Delta\theta \rightarrow 0^+$). The radii of these two compression wavelets are $r(\theta, t)$ and $r(\theta + \Delta\theta, t)$, respectively. Similar to (2.5) and (2.6), the emission angle α_θ , which is the angle between the vector of the emitted ray and the tangent vector of the water column at P_θ , can be derived as

$$\begin{aligned} \cos \alpha_\theta &= \lim_{\Delta\theta \rightarrow 0^+} \left[\frac{(2t - t_\theta - t_{\theta+\Delta\theta})(t_{\theta+\Delta\theta} - t_\theta)c_{l,0}}{2(t - t_\theta) R_D \Delta\theta} \frac{\Delta\theta/2}{\sin(\Delta\theta/2)} + \frac{R_D \sin(\Delta\theta/2)}{(t - t_\theta)c_{l,0}} \right] \\ &= \lim_{\Delta\theta \rightarrow 0^+} \frac{(t_{\theta+\Delta\theta} - t_\theta)c_{l,0}}{R_D \Delta\theta} = \frac{c_{l,0}}{R_D} t'_\theta = \frac{\kappa}{M_\theta} \frac{(\omega - 1) \sin \theta}{\sqrt{1 + (\omega - 1)^2 + 2(\omega - 1) \cos \theta}}, \end{aligned} \quad (3.6)$$

Curved shock interaction with water column

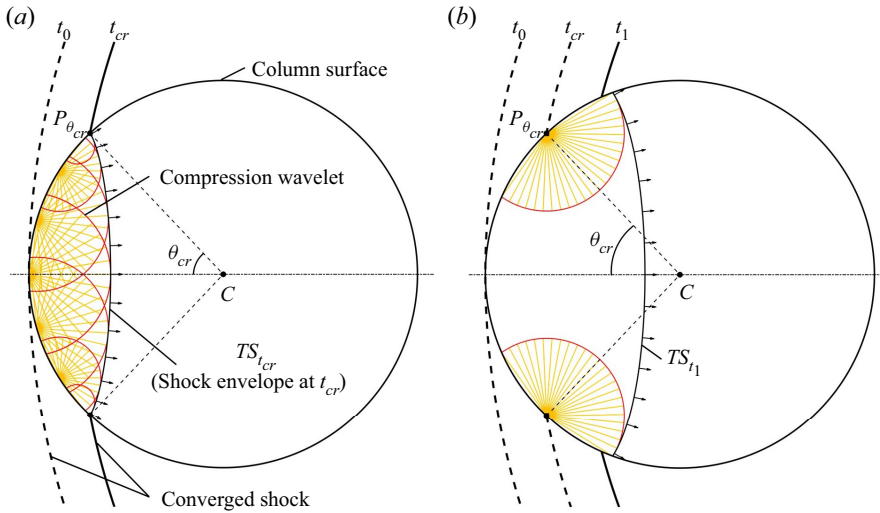


Figure 10. Schematic diagram of the generation of transmitted shock wave and the ray analysis: (a) the schematic diagram at critical time t_{cr} ; (b) the schematic diagram at the time instant t_1 , selected after the critical time.

where the dimensionless parameter κ represents the ratio of the sound speed of water to that of air. It is worth noticing that, for the interactions of a planar shock wave (the radius ratio ω tends to the infinite and the incident shock intensity is a constant M_0) with a water column, the angle α_θ satisfies $\cos \alpha_\theta = \kappa \sin \theta / M_0$. This theoretical result is the same as the acoustic principle used by Biasiori-Poulanges & El-Rabii (2021) in studying the interaction between a planar shock wave and a water column. According to (3.4), it can be concluded that $\alpha_{\theta_{cr}}$ of the ray generated by the critical contact point $P_{\theta_{cr}}$ equals zero. That is to verify that when $t > t_{cr}$, the transmitted shock wave presents a precursory characteristic. Only one particular ray out of the infinite number of rays generated by the same contact point, whose emission angle satisfies (3.6), effectively influences the envelope of compression wavelets. Hence, only these specific rays emitted from different contact points ($\theta > \theta_{cr}$) are considered and analysed in the subsequent analysis, and the influence of the other rays is ignored.

As the transmitted shock wave propagates forwards, the reflected rarefaction waves are observed behind the transmitted shock and a certain time, t ($t^* = 0.8695$) is chosen for the following analysis, figure 11(a, b). The position and shape of the reflected rarefaction waves are obtained from the analysis of the emitted rays. Meanwhile, it is assumed that the rays will be reflected symmetrically on the curved column surface (Wu *et al.* 2018). At a specific instant t , the length of the ray emitted by the contact point P_θ is $r(\theta, t)$. Moreover, if the ray is reflected from the water column surface, r will represent the total length of the ray before and after reflection. Furthermore, the ray could be reflected more than once from the column surface, and the reflection times are related to the contact angle θ and the time t , which are elaborated as follows.

If the rays emitted from P_θ are not reflected at an instant t , the emitting angle α_θ will satisfy the following:

$$\alpha_\theta \geq \arcsin \frac{r(\theta, t)}{2R_D} = \arcsin \left[\left(t - \int_0^\theta \frac{L'_\xi}{M_\xi c_{g,0}} d\xi \right) \frac{c_{l,0}}{2R_D} \right] = \alpha_\theta^{(1)}, \quad (3.7)$$

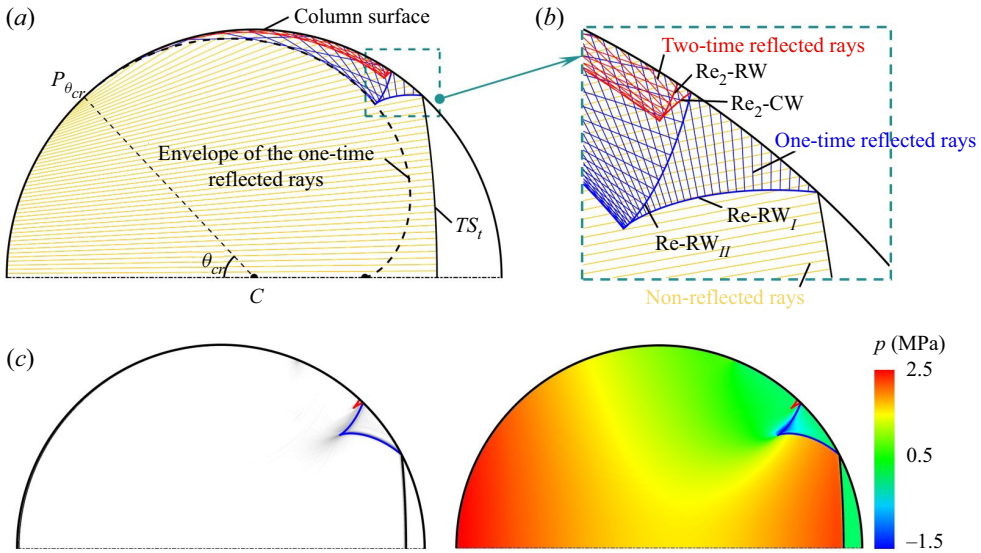


Figure 11. The schematic diagram of the ray analysis: (a) the schematic diagram at $t^* = 0.8695$; (b) the enlarged view of the schematic diagram at t . (c) The comparison of results between ray analysis and numerical simulation at $t^* = 0.9543$.

where L'_θ represents the derivative of the equivalent propagation distance L_θ of the curved shock along the symmetrical axis of the water column for the contact angle θ

$$L'_\theta = \frac{(\omega - 1) \sin \theta}{\sqrt{1 + (\omega - 1)^2 + 2(\omega - 1) \cos \theta}} R_D. \quad (3.8)$$

If the rays are reflected N times ($N = 1, 2, 3, \dots$), angle α_θ will satisfy

$$\alpha_\theta < \arcsin \frac{r(\theta, t)}{2NR_D} = \arcsin \left[\left(t - \int_0^\theta \frac{L'_\xi}{M_\xi c_{g,0}} d\xi \right) \frac{c_{l,0}}{2NR_D} \right] = \alpha_\theta^{(N)}, \quad (3.9)$$

$$\alpha_\theta \geq \arcsin \frac{r(\theta, t)}{2(N+1)R_D} = \arcsin \left[\left(t - \int_0^\theta \frac{L'_\xi}{M_\xi c_{g,0}} d\xi \right) \frac{c_{l,0}}{2(N+1)R_D} \right] = \alpha_\theta^{(N+1)}. \quad (3.10)$$

Thus, the emission angle α_θ can be divided into different intervals according to reflection times N , and the intervals of angle θ can be obtained by combining with (3.6).

Due to the specific column surface, the reflected rarefaction wave has two branches: the far branch (Re-RW_{II}) and the near branch (Re-RW_I), as judged by the distance of the branch from the axis of the water column. Similarly, the reflected rarefaction will also reflect on the water column surface and forms the second reflected wave, it has two branches with entirely different properties: the second reflected compression wave (Re₂-CW) and the second reflected rarefaction wave (Re₂-RW). It deviates from the statement (Xiang & Wang 2017; Wu *et al.* 2018) that the second reflection forms the compression wave with a single characteristic, but the phenomenon obtained by the present study is consistent with the experimental result of Sembian *et al.* (2016). Nonetheless, we will not elaborate further on this in the present study.

The comparison of results between ray analysis and numerical simulation at $t^* = 0.9543$ is shown in figure 11(c), and more details about the comparison between the numerical

Curved shock interaction with water column

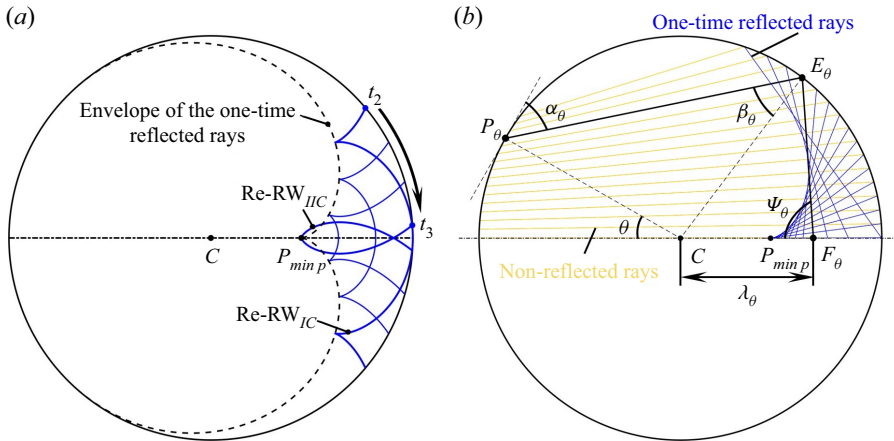


Figure 12. (a) Schematic diagram of the first reflected expansion wave propagation from t_2 ($t^* = 1.0$) to t_3 ($t^* = 1.2698$); (b) schematic diagram of ray analysis for the focusing of the one-time reflected rays.

simulation results and theoretical results are presented in [Appendix C](#). It is obvious that the shape and position of wave structures obtained by theoretical analysis almost coincide with the distribution of wave structures in the numerical results. Hence, this verifies the reliability and accuracy of the theoretical analysis in predicting the motion characteristics of the wave structures. Moreover, due to the strong stretched effect, a negative-pressure region is found near the intersection of two branches of the first reflected rarefaction wave. Meanwhile, the pressure behind the far branch of the first reflected rarefaction waves is quickly recovered because the subsequently emitted compression wavelets catch up with these two rarefaction wave branches.

3.2. The first convergence of the first reflected rarefaction wave

The first stage ends when the transmitted shock wave reaches the right pole of the water column at the time instant t_2 ($t^* = 1.0$), and the second stage begins. At this moment, the transmitted shock wave is completely reflected, and two near branches of the reflected rarefaction wave on both sides of the central axis of the water column merge, forming a continuous converged rarefaction wave (Re-RW_{IC}). The analytical schematic is presented in [figure 12\(a\)](#), which demonstrates the first reflected rarefaction wave evolution. It is observed that the intersection points of Re-RW_{II} and Re-RW_I move along the envelope of the one-time reflected rays from time t_2 to t_3 , and the continuous reflected rarefaction wave (Re-RW_{IC}) gradually focuses inside the water column. When Re-RW_{IC} completely focuses, the two branches of the far-branch rarefaction wave meet and form a continuous diverged rarefaction (Re-RW_{IIC}).

Previous studies (Sembian *et al.* 2016; Xiang & Wang 2017; Wu *et al.* 2018; Biasiori-Poulanges & El-Rabii 2021) have found that the complete focus of the reflected rarefaction wave decreases the water pressure rapidly, and the maximum negative pressure inside the water column reaches approximately -10 MPa at the complete focus instant. The pressure distributions along the centre axis of the water column, just before and after the complete focus instant, are presented in [figure 13](#), and it can be seen that a similar focusing pressure (-10 MPa) is obtained in the present study. This extremely negative pressure has far exceeded the cavitation threshold pressure of -2.3 MPa of unpurified water reported by Sembian *et al.* (2016). Therefore, the region inside the water near the

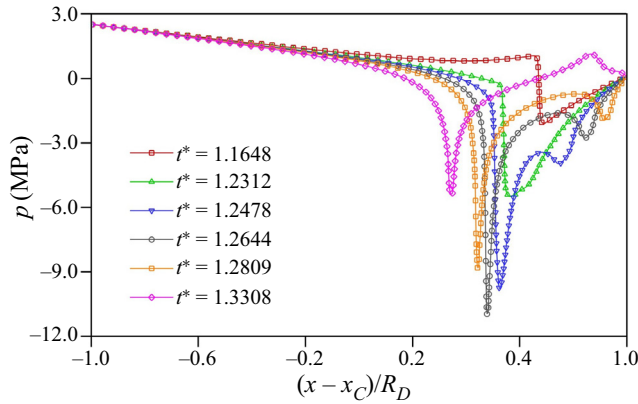


Figure 13. The pressure distribution along the centre axis of the water column, just before and after the complete focus instant, for the interaction between the cylindrical converged shock and the water column.

focus point has a high probability of capturing the cavitation phenomenon. Hence, the focus point of the first reflected rarefaction wave is called the cavitation kernel point in the present study, denoted as P_{cav} . Combined with figure 12(b), P_{cav} is also the left limiting position of the one-time reflected rays that intersect with the central axis of the water column.

The position of P_{cav} can be obtained theoretically according to the ray analysis (Obreschkow *et al.* 2011; Wu *et al.* 2018; Biasiori-Poulanges & El-Rabii 2021) considering the planar incident shock wave or flat rigid surface. Here, we present the case analysis considering the curved, cylindrical, incident shock wave.

Some rays emitted by the contact point whose contact angle is less than the critical contact angle θ_{cr} are presented in figure 12(b). In order to ensure that the one-time reflected rays can intersect with the horizontal central axis, the emission angle α_θ and the contact angle θ will satisfy $4\alpha_\theta + \theta > 180^\circ$. Selecting an arbitrary ray (the black solid lines) for analysis, the intersection points of the one-time reflected part of this ray with the column surface and the horizontal central axis are E_θ and F_θ , respectively. And the distance λ_θ from F_θ to the column centre can be expressed as follows:

$$\lambda_\theta = \frac{\sin \beta_\theta}{\sin \psi_\theta} R_D = \frac{R_D}{\sin \theta \sin \alpha_\theta (4 \cos \alpha_\theta - 1 / \cos \alpha_\theta) + \cos \theta (3 - 4 \cos^2 \alpha_\theta)}. \quad (3.11)$$

After substituting (3.6) into (3.11) and simplifying, the expression of distance λ_θ can be rewritten as follows:

$$\lambda_\theta = \frac{R_D}{F_1(\theta) - F_2(\theta) + F_3(\theta)}, \quad (3.12)$$

where, $F_1(\theta)$, $F_2(\theta)$ and $F_3(\theta)$ are shown as

$$F_1(\theta) = \frac{4\kappa(\omega - 1)\sin^2 \theta}{\sqrt{1 + (\omega - 1)^2 + 2(\omega - 1)\cos \theta} M_\theta} \sqrt{1 - \frac{\kappa^2(\omega - 1)^2 \sin^2 \theta}{[1 + (\omega - 1)^2 + 2(\omega - 1)\cos \theta] M_\theta^2}}, \quad (3.13)$$

$$F_2(\theta) = \frac{M_\theta \sqrt{1 + (\omega - 1)^2 + 2(\omega - 1) \cos \theta}}{\kappa(\omega - 1)} \sqrt{1 - \frac{\kappa^2(\omega - 1)^2 \sin^2 \theta}{[1 + (\omega - 1)^2 + 2(\omega - 1) \cos \theta] M_\theta^2}}, \quad (3.14)$$

$$F_3(\theta) = 3 \cos \theta - \frac{4\kappa^2(\omega - 1)^2 \sin^2 \theta \cos \theta}{[1 + (\omega - 1)^2 + 2(\omega - 1) \cos \theta] M_\theta^2}. \quad (3.15)$$

A maximum limiting value of λ_θ exists. Accordingly, the position of P_{cav} , as well as the focus point of the one-time reflected rays, is obtained, which has the following expression:

$$\frac{\lambda_{max}}{R_D} = \lim_{\theta \rightarrow 0} \frac{\lambda_\theta}{R_D} = \frac{1}{\lim_{\theta \rightarrow 0} F_1(\theta) - \lim_{\theta \rightarrow 0} F_2(\theta) + \lim_{\theta \rightarrow 0} F_3(\theta)} = \frac{\kappa}{3\kappa - M_0 f_s}, \quad (3.16)$$

where $f_s = \omega/(\omega - 1)$ is the function characterising the effect of shock wave shapes in the case of the cylindrical converged incident shock wave.

The above expression has indicated that the relative distance from the cavitation kernel point P_{cav} to the column centre is determined by three dimensionless parameters: the shock Mach number M_0 , the radius ratio ω between the cylindrical converged shock wave and the water column and the sound-speed ratio κ between the water and the air. If the radius ratio tends to the infinite, the cylindrical converged shock wave degenerates into a planar one. Here, we define a new dimensionless parameter $n = \kappa/M_0$, which represents the ratio of the wave speed between the transmitted shock wave and the incident shock wave. The distance x_f from the focus point P_{cav} to the centre of the water column can be written as

$$x_f = \frac{n}{3n - 1} R_D, \quad (3.17)$$

which is then identical to the expression reported by Biasiori-Poulanges & El-Rabii (2021). In other words, the theoretical analysis derived in this paper is universal for different incident shock wave shapes.

3.3. The second convergence of the second reflected waves

When Re-RW_{IC} completely focuses, the continuous diverged rarefaction wave (Re-RW_{IC}) propagates upstream of the water column and is reflected by the column surface, forming the second reflected compression wave (Re₂-CW) and the second reflected rarefaction wave (Re₂-RW). Due to the specific column surface, the one branch of the second reflected wave (Re₂-CW) firstly focuses on the central axis of the water column, P_{tran} , causing a high-pressure region whose maximum pressure reaches more than 60 times the initial pressure, as shown in figure 7(k). After an extremely short time, the two symmetrical reflected rarefaction waves (Re₂-RW), located on the upper and lower sides of Re₂-CW, merge and cause a rapid decrease in the local pressure. The pressure distribution along the centre axis of the water column at six different time instants, before and after the focus of Re₂-CW, is shown in figure 14. Obviously, the maximum pressure in the high-pressure region increases rapidly as the focus process continues before the complete focussing of Re₂-CW. After that, a significant negative-pressure region appears inside the water column, and the maximum pressure in the high-pressure region decreases rapidly and then disappears.

The evolution characteristics of the second reflected wave from t_4 ($t^* = 2.0$) to t_5 ($t^* = 2.326$) based on the ray analysis are shown in figure 15(a). Due to the different properties

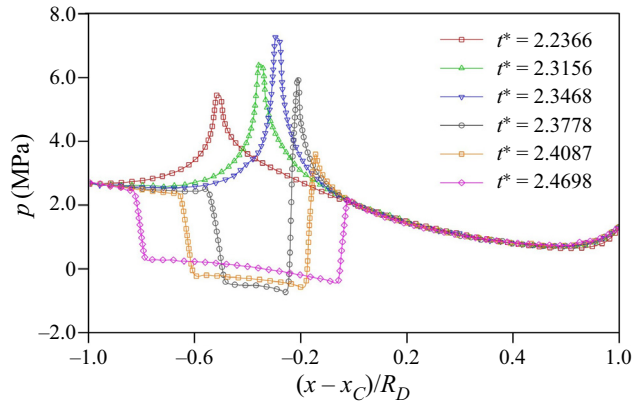


Figure 14. The pressure distribution along the centre axis of the water column at six different time instants for the interaction between the cylindrical converged shock and the water column.

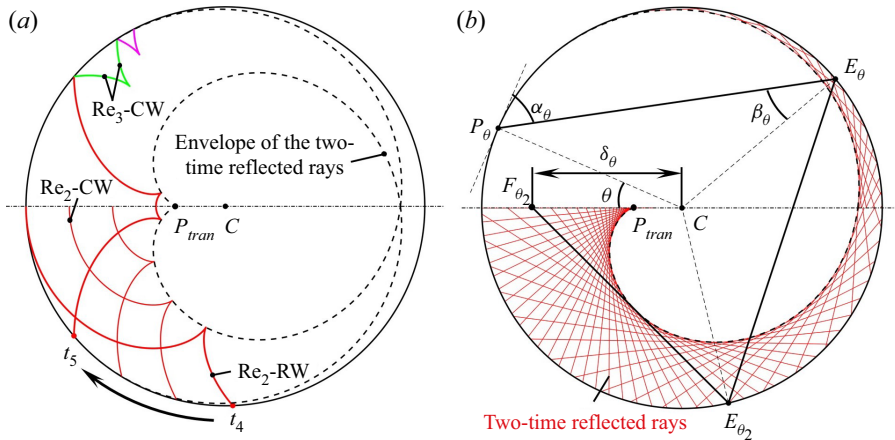


Figure 15. (a) Schematic diagram of the second reflected wave propagation from t_4 ($t^* = 2.0$) to t_5 ($t^* = 2.326$) and schematic diagram of shapes and positions of the reflected waves at time t_5 ; (b) schematic diagram of ray analysis for the intersection point between the reflected rays, with two-time reflection, and the central axis of the water column.

of the two branches of the second reflected wave, the liquid near P_{tran} undergoes a violent pressure oscillation in a short time interval. The highly transient characteristics of liquid pressure have great significance in the biomedical field, which is a valuable measure to remove diseased tissue. Similar to the derivation of P_{cav} , the specific position of P_{tran} can be obtained by the ray analysis. A schematic diagram of rays emitted from some contact points when Re_2 -CW focuses is shown in figure 15(b), selecting an arbitrary ray (the black lines) for further analysis. Denoting the intersection points of the two-time reflected part of this ray with the column surface and the central axis of the water column as E_{θ_2} and F_{θ_2} , respectively, with the distance from F_{θ_2} to C being δ_{θ} ,

$$\delta_{\theta} = \frac{\sin \beta_{\theta}}{\sin(\pi - 5\beta_{\theta} + \theta)} R_D = \frac{\cos \alpha_{\theta}}{\cos(5\alpha_{\theta} + \theta)} R_D. \quad (3.18)$$

After substituting (3.6) into (3.18) and simplifying, the minimum distance of δ_θ can be obtained as δ_{min} , which has the following expression:

$$\frac{\delta_{min}}{R_D} = \lim_{\theta \rightarrow 0} \left[\frac{\cos \alpha_\theta}{(16 \cos^4 \alpha_\theta - 20 \cos^2 \alpha_\theta + 5) \cos \alpha_\theta \cos \theta - (16 \cos^4 \alpha_\theta - 12 \cos^2 \alpha_\theta + 1) \sin \alpha_\theta \sin \theta} \right] = \frac{\kappa}{5\kappa - M_0 f_s} \tag{3.19}$$

Moreover, to ensure that the two-time reflected rays can intersect with the horizontal central axis before it is reflected from the column surface, the emission angle α_θ and the contact angle θ will satisfy: $6\alpha_\theta + \theta < 360^\circ$. It is easy to find that, as the reflection time increases, the maximum contact angle of rays participating in the focus process gradually decreases. This means that fewer rays participate in the focusing process with the interaction process continuing, which makes the reflected wave and focus intensity weaker and weaker.

Similar to the transmitted shock wave and the first reflected rarefaction wave, the second reflected waves also reflect on the column surface, forming the third reflected compression wave, figure 15(a), which will focus inside the water column causing a high-pressure region. As the interaction continues, the high-pressure and low-pressure areas appear alternately at different positions on the centreline. Their analysis procedure is similar to the focusing of the first reflected expansion wave and the second reflected compression wave. The following expression gives a general formula of the distance from the focusing point $x_{f,N}$ of the N times reflected wave to the column centre:

$$\frac{x_{f,N}}{R_D} = \frac{\kappa}{(2N + 1)\kappa - M_0 f_s}, \quad N = 1, 2, 3, \dots \tag{3.20}$$

However, the intensity of these waves, with three times or more reflection, has been dramatically reduced compared with the intensity of the transmitted shock wave, the first reflected rarefaction wave and the second reflected wave. Therefore, we will not elaborate further in the present study.

4. The effect of incident shock wave shapes and intensities

In addition to converged shock waves, diverged shock waves also widely interact with the gas–liquid interface in nature, industrial production and scientific research, such as the interaction of a blast wave with a droplet. The derivation for the interaction of a diverged cylindrical shock wave with a water column, figure 16, is similar to that of a converged cylindrical shock wave with a water column, which is introduced in § 3. Again, the initial shock wave Mach number $M_0 = 2.4$ and radius ratio $\omega = 4.0$ of the diverged cylindrical shock are chosen in the following analysis, and (3.1) and (3.2) for the interaction between the diverged shock and the water column can be rewritten as the following expressions:

$$R_\theta = R_D \sqrt{1 + (\omega + 1)^2 - 2(\omega + 1) \cos \theta}, \tag{4.1}$$

$$\sin \chi = \frac{(\omega + 1) \sin \theta}{\sqrt{1 + (\omega + 1)^2 - 2(\omega + 1) \cos \theta}}. \tag{4.2}$$

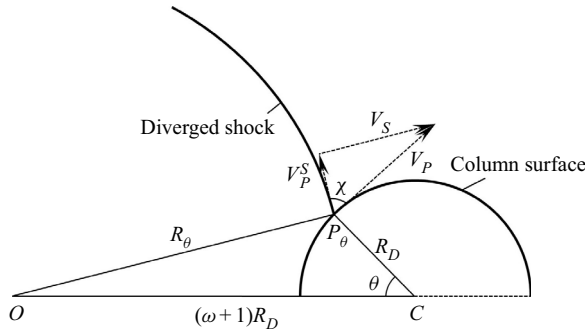


Figure 16. Schematic diagram of the interaction between the cylindrical diverged shock wave and the water column.

The critical contact angle θ_{cr} , when the transmitted shock wave just detaches from the incident diverged shock wave and the reflected shock wave, can be obtained as follows:

$$\frac{\sqrt{1 + (\omega + 1)^2 - 2(\omega + 1) \cos \theta_{cr}}}{(\omega + 1) \sin \theta_{cr}} = \frac{c_{l,0}}{M_{\theta_{cr}} c_{g,0}}. \quad (4.3)$$

In the case of $M_0 = 2.4$, the value of θ_{cr} for the diverged shock wave ($\omega = 4.0$) is 28.3° compared with $\theta_{cr} = 44.9^\circ$ for the converged shock wave ($\omega = 4.0$) and $\theta_{cr} = 35.1^\circ$ for the planar shock wave. The critical contact angle is compared in table 1 with the analytical and numerical results of the three configurations at different incident shock wave intensities and shapes. The simulation results agree with the analytical values. Meanwhile, compared with the interaction between the planar shock wave and the water column, the converged shock wave will delay the percussive behaviour of the transmitted shock wave, while the diverged shock wave will accelerate the appearance of this phenomenon. Similarly, the time t_θ , which represents the time of contact point moving from the left pole of the water column to P_θ , and the emission angle α_θ at P_θ can be rewritten as follows:

$$t_\theta = \int_0^\theta \frac{(\omega + 1) \sin \xi R_D}{\sqrt{1 + (\omega + 1)^2 - 2(\omega + 1) \cos \xi} M_\xi c_{g,0}} d\xi, \quad (4.4)$$

$$\cos \alpha_\theta = \frac{c_{l,0}}{R_D} t'_\theta = \frac{\kappa}{M_\theta} \frac{(\omega + 1) \sin \theta}{\sqrt{1 + (\omega + 1)^2 - 2(\omega + 1) \cos \theta}}. \quad (4.5)$$

Further, the location of the cavitation kernel point P_{cav} for a diverged shock interacting with a water column can be obtained by the ray analysis, and the distance from P_{cav} to the water column centre C is also denoted as λ_{max}

$$\frac{\lambda_{max}}{R_D} = \lim_{\theta \rightarrow 0} \frac{\lambda_\theta}{R_D} = \frac{\kappa}{3\kappa - M_0 f_s}, \quad (4.6)$$

where $f_s = \omega/(\omega + 1)$ is the function characterising the effect of shock wave shapes in the case of the cylindrical diverged incident shock wave.

Hence, considering (3.16), (4.6) and the formula for the interaction of the planar shock with a water column reported by Biasiori-Poulanges & El-Rabii (2021), the function f_s characterising the effect of shock wave shapes can be rewritten in a unified form, that is $f_s = \omega/(\omega - \varepsilon)$. Here, ε represents the types of incident shock shape (-1 represents the diverged shock, 0 represents the planar shock and 1 represents the converged shock).

		Converged shock wave $\omega = 4.0$	Planar shock wave $\omega = \infty$	Diverged shock wave $\omega = 4.0$
$M_0 = 1.6$	Numerical	29.8°	22.5°	18.0°
	Theoretical	30.0°	22.5°	18.1°
$M_0 = 2.0$	Numerical	38.0°	28.6°	22.8°
	Theoretical	38.1°	28.6°	23.0°
$M_0 = 2.4$	Numerical	44.6°	34.9°	28.2°
	Theoretical	44.9°	35.1°	28.3°
$M_0 = 3.0$	Numerical	60.7°	45.7°	36.8°
	Theoretical	61.3°	45.9°	37.1°

Table 1. The critical contact angle θ_{cr} values at different incident shock wave intensities and shapes.

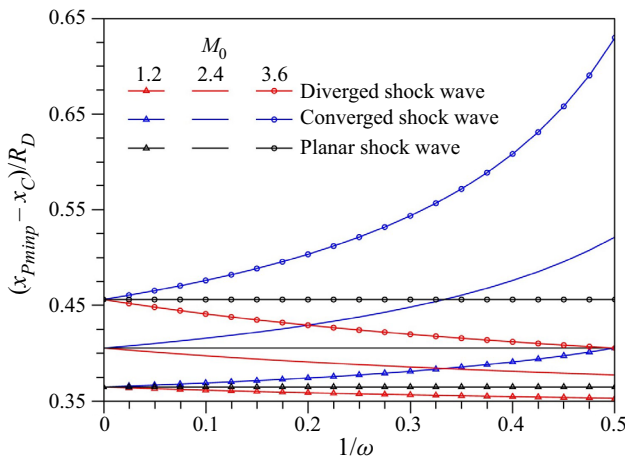


Figure 17. The position of P_{cav} for theoretical analysis for three incident shock wave shapes and three incident shock wave intensities varies with the dimensionless radius ω .

It can be found that the factors affecting the relative position of P_{cav} can be divided into two parts. One part is the physical parameter, including property parameters of the two-phase system that affects the value of κ and the initial strength of the incident shock wave that affects the value of M_0 . Another part is the geometrical parameter which affects the value of the initial radius ratio ω if the curved shock wave has a cylindrical shape. A detailed analysis will be introduced in our further works when the shape of the curved shock wave is not as perfect as that of a cylindrical shock wave. Figure 17 presents the position of P_{cav} for theoretical analysis of three incident shock wave shapes and three incident shock wave intensities varying with the dimensionless radius ω . It can be found that the position of P_{cav} , in the case of the converged shock, will be obviously offset with the increase of the incident shock wave curvature $1/\omega$, while its offset direction is opposite to that in the case of the diverged shock. Therefore, we can use a weaker converged shock to obtain the same focus point of the reflected rarefaction wave compared with the cases of the planar shock wave.

The comparison of the numerical result at $M_0 = 2.4$ for three different shapes of the incident shock wave is shown in figure 18. It can be found that the converged shock wave can delay the reflection transition of the incident shock wave from the regular reflection to the irregular Mach reflection, while the diverged shock wave can promote this process, as

shown in [figure 18\(b\)](#). The pressure contours inside the water column for three different shapes of incident shock waves at their respective focus instants are shown in [figure 18\(c\)](#). The minimum pressure–time curves inside the water column for three different types of incident shock waves are shown in [figure 19](#). It is noticed that the converged shock wave can significantly enhance the phenomenon of the negative pressure induced by the focus of the reflected rarefaction wave. In contrast, the diverged shock can observably restrain this negative-pressure phenomenon. In other words, for a certain purity of water, a maximum probability of cavitation exists in the interactions of the converged shock wave with a water column and a minimum probability of cavitation exists in the interactions of the diverged shock wave with a water column compared with the interactions of the planar shock wave with a water column. The main reason is that the larger critical angle makes the envelope of the transmitted shock wave have a larger ray density and brings a significant negative pressure. Similarly, the pressure oscillation (the difference between the maximum and minimum pressure) caused by the focus of the second reflected wave (Re₂-EW and Re₂-CW) is more apparent in the case of the converged shock wave, [figure 19](#).

However, by observing [figure 18\(d\)](#), it can be found that the negative pressure inside the water column, caused by the second reflected rarefaction wave, is much more significant in the case of the diverged shock wave than that in the case of the converged shock wave. It is worth noting that the focus of Re₂-CW would not generate a sharp high-pressure peak in the case of the diverged shock wave and the planar shock wave, which appears in the case of the converged shock wave. The main reason is that, as the interaction continues, the intensity of the incident shock wave gradually increases in the case of the converged shock wave. Hence, the pressure behind the reflected rarefaction recovery is quicker than in the other two cases. Moreover, [figure 19](#) also shows that the time required for the reflected rarefaction wave to focus completely is the lowest under the converged shock wave, while it reaches the maximum under the diverged shock wave. In conclusion, the converged shock wave can significantly enhance the probability of cavitation inside the water column and simultaneously shorten the distance from the focus point P_{cav} to the column centre.

Previous studies in interactions of the planar shock wave with a water column (Sembian *et al.* 2016; Xiang & Wang 2017; Biasiori-Poulanges & El-Rabii 2021) have shown that, with the increase of the incident shock wave intensity, there is a stronger negative-pressure effect caused by the first reflected rarefaction wave and a greater possibility of cavitation. In this section, we will determine how the initial shock wave intensity of different shapes of the incident curved shock wave influences the interaction process.

[Figure 20\(a\)](#) presents the minimum pressure p_{min} during the focus of Re-RW_{IC} for three incident shock wave shapes varying with shock wave intensity in the range of 1.2–4.5. A few trends stand out. One is that p_{min} decreases rapidly as the shock intensity increases, and p_{min} is always negative for all shock wave intensities. Additionally, the minimum pressure induced by the converged shock wave is always lower than that induced by the planar shock wave and the diverged shock wave, and this phenomenon becomes apparent at a higher shock wave intensity. In addition, the cavitation threshold pressure obtained from Sembian *et al.* (2016) is added in [figure 20\(a\)](#). It can be found that p_{min} is supposed to exceed the cavitation threshold if the shock wave intensity is large enough. In other words, the stronger the incident shock wave intensity, the higher the cavitation possibility. Because the focus pressure is the lowest in the case of the converged shock wave, the converged shock wave can significantly enhance the cavitation possibility. The comparison of the position of P_{cav} (p_{minp}) between theoretical analysis and numerical simulations for different incident shock wave shapes is shown in [figure 20\(b\)](#). It can be seen that, no matter what shape the incident shock wave is, the distance from P_{cav} (p_{minp}) to the column

Curved shock interaction with water column

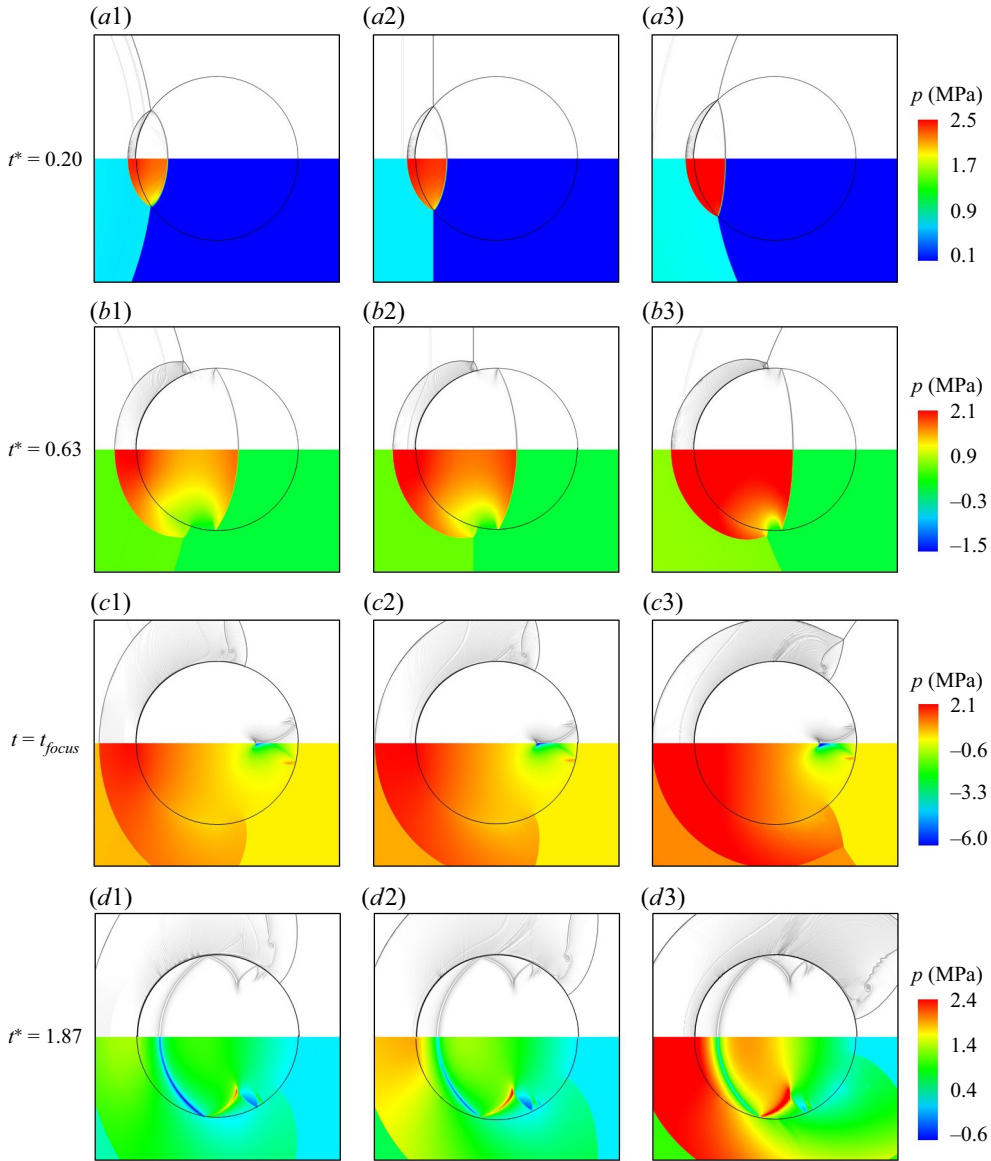


Figure 18. The comparison of the numerical results of the interaction between the shock wave and a water column, $M_0 = 2.4$, for three different types of the shape of the incident shock wave (1 represents the diverged shock wave, 2 represents the planar shock wave and 3 represents the converged shock wave).

centre C increases as the shock wave intensity increases both in theoretical analysis and numerical simulations. In addition, compared with cases of the planar shock wave, an obvious left shift, decreasing the distance, is found in cases of the diverged shock wave, while a considerable right shift, increasing the distance, is found in cases of the converged shock wave. The numerical simulations show a similar trend to the theoretical analysis, although it is worth noticing that the theoretical focus point of the first reflected rarefaction wave P_{cav} does not coincide with the minimum pressure point p_{minp} in the numerical results, also presented by Biasiori-Poulanges & El-Rabii (2021). This deviation between

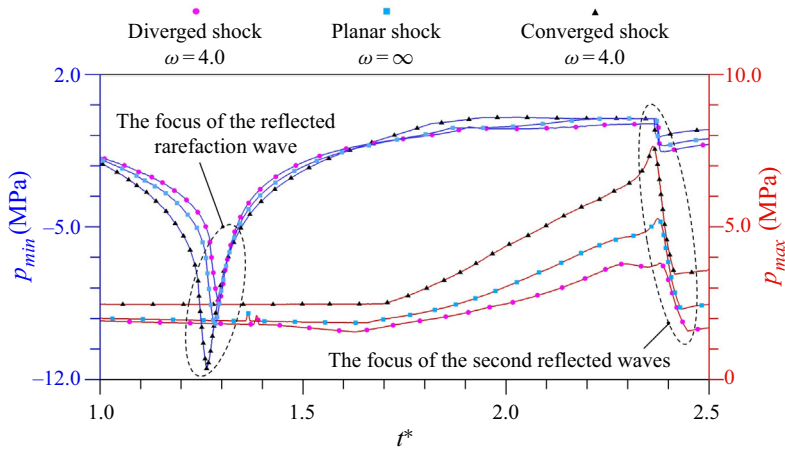


Figure 19. The evolution of the minimum and maximum pressures inside the water column over time for three incident shock wave shapes, $M_0 = 2.4$.

the theoretical analysis and numerical simulations is mainly caused by the assumption of the infinitely thin wave structures in the theoretical analysis. However, this assumption of discontinuity in mathematics does not exist in numerical simulations and experiments. Hence, if a higher prediction accuracy of the theoretical analysis is expected, the effect of wave width must be considered, but it is still hard to achieve in a short time. To this end, a balanced approach, which means the assumption of the infinitely thin wave structures is kept in the theoretical analysis, but the effect of grid size on predicting the position of the focusing point is considered, is used to verify our explanation as also shown in figure 20(b). It can be found that the deviation between theoretical results and numerical simulations decreases significantly if the effect of grid size is considered. Of course, the velocity estimation of the transmitted shock wave will also lead to a difference in the P_{cav} position between the theoretical analysis and numerical simulations. Nonetheless, the theoretical results obtained in the present study still have a high accuracy in predicting the focus of reflected waves and the region with high cavitation possibility inside the water column.

5. Conclusion

In this paper, we examined the early stage of the interaction of the curved shock wave with a cylindrical water column emphasising the analysis of waves that are converging. The study was conducted using the ray analysis method complemented by numerical simulations.

The spatio-temporal evolution and interaction of the complicated waves inside the water column have been detailed when the cylindrical converged, cylindrical diverged and planar shock waves are considered. The transmitted shock wave is generated inside the water column immediately after the impact of the shock wave. When the contact angle θ is larger than the critical value θ_{cr} , the transmitted shock wave will detach from the incident shock wave, forming the precursor shock wave. The value of θ_{cr} is determined by the incident shock wave intensity, the sound-speed ratio of the two phases and the shapes of the incident shock. Meanwhile, although there are countless rays on the same compression wavelet, only one ray, whose emission angle α_θ satisfies (3.6), will affect the envelope of compression wavelets. After the detachment, the precursor shock wave propagates and

Curved shock interaction with water column

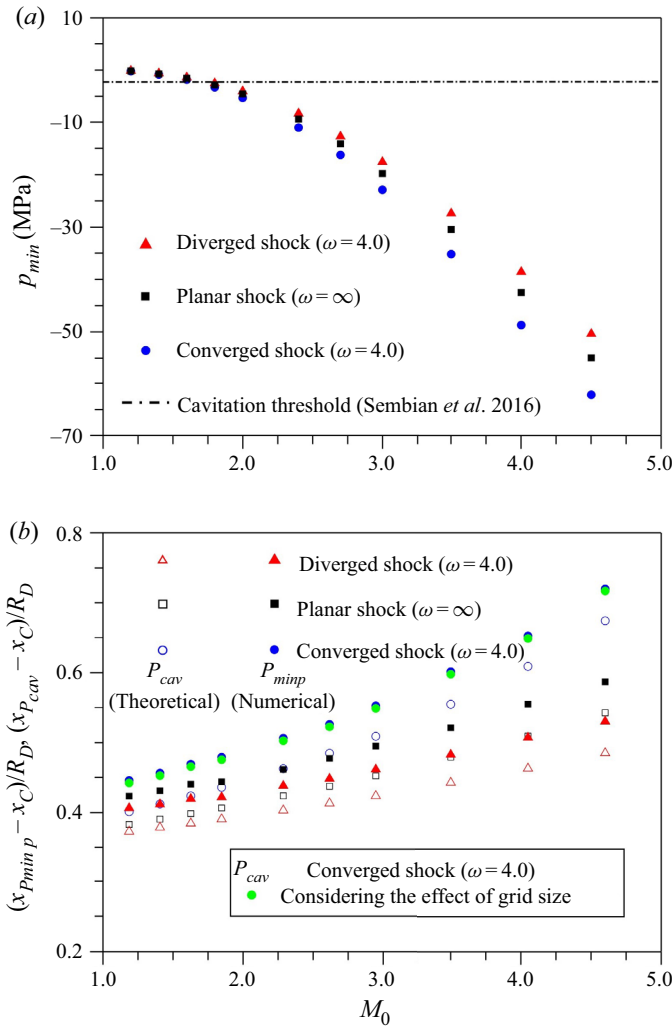


Figure 20. (a) The minimum pressure p_{min} during the focusing of Re-RW_{IC} for three incident shock wave shapes varies with shock wave intensity. (b) The focus point position for theoretical prediction (P_{cav}) and numerical simulation (p_{minp}) for three incident shock wave shapes varies with shock wave intensity.

transiently reflects from the column surface, generating a series of rarefaction waves. The focus of the reflected rarefaction wave can induce negative-pressure regions, where a higher probability of cavitation exists if the wave strength is high enough. In addition, a highly transient pressure oscillation is observed near the focus region of the second reflected wave, whose two branches have opposite properties. Based on the ray analysis, the positions of the focusing points of the first reflected rarefaction wave and the second reflected wave are derived, as determined by the dimensionless sound speed κ , the initial shock wave intensity M_0 and the dimensionless function f_s characterising the effect of shock wave shapes.

The present study also investigates the effects of the initial shock wave intensity and the shapes of the incident shock wave. It is found that, due to having a larger critical detachment angle θ_{cr} that will bring a larger ray density to the compression wavelet

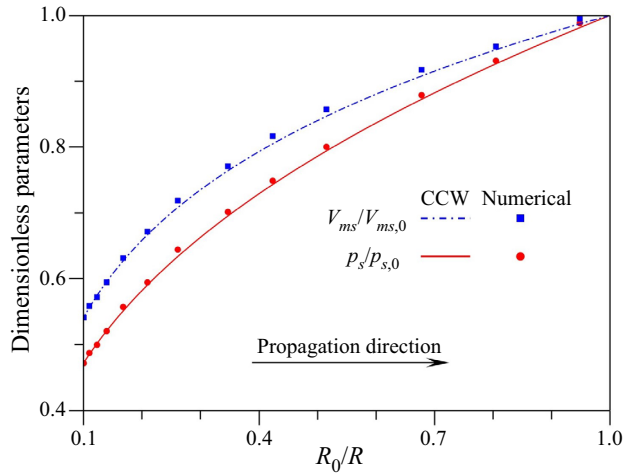


Figure 21. The comparison of dimensionless parameters of the cylindrical shock wave varying with different shock radii between the CCW theory and numerical simulation.

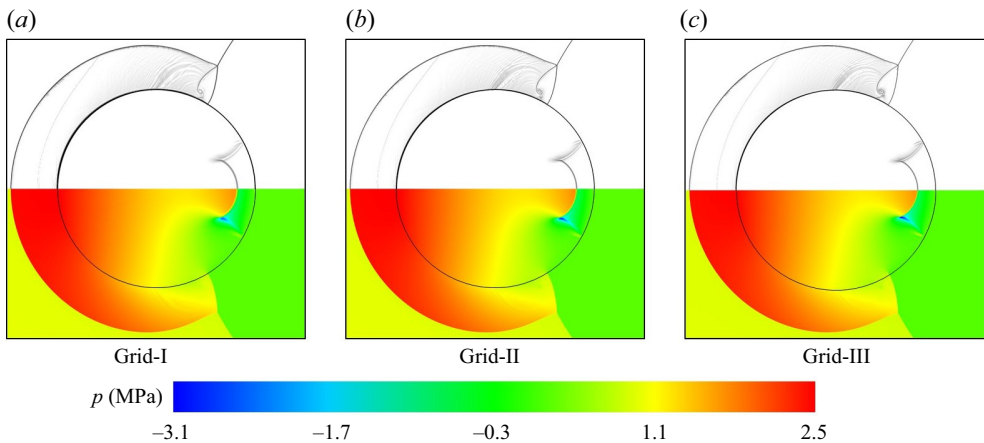


Figure 22. The numerical schlieren (top) and pressure (bottom) contours of the three different grid resolutions at $t = 3.6 \mu\text{s}$, $\omega = 4.0$ and $M_0 = 2.4$.

envelope, the converged shock wave envelope induces a stronger negative pressure and a stronger pressure oscillation inside the water column, while the diverged shock wave, having a smaller detachment critical angle, weakens these phenomena. However, due to a rapid pressure recovery after the reflected rarefaction wave, the diverged shock wave can induce a significant secondary negative-pressure effect when the second reflected wave focuses inside the water column, compared with the other two shapes of the incident shock wave. In addition, the converged shock wave can shorten the distances from the focus points to the column centre, enhancing the probability of cavitation inside the water column. It is undoubtedly the case that the diverged shock wave increases these distances and weakens the cavitation probability. Based on the above analysis, the wave structure evolution mechanism and essential influencing factors can contribute to practical applications, such as fuel droplet atomisation under the interaction of a cellular

Curved shock interaction with water column

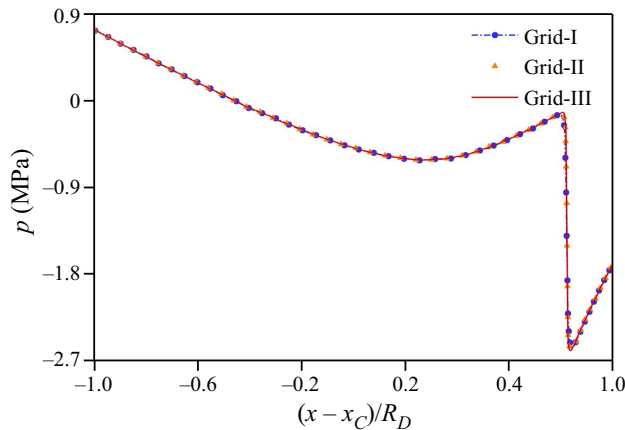


Figure 23. Pressure distribution along the symmetrical axis of the water column under three different grid resolutions at $t = 3.6 \mu\text{s}$, $\omega = 4.0$ and $M_0 = 2.4$.

detonation wave. Future work will further investigate the cavitation behaviours induced by the rarefaction waves during the curved shock wave and the droplet interactions.

Funding. This work is partially supported by the National Natural Science Foundation of China (grant nos 91952205, 12002039) and the National Science and Technology Major Project of China (grant nos 2017-I-0004-0004, 2017-III-0005-0030), respectively.

Declaration of interests. The authors report no conflict of interest.

Author ORCIDs.

-  Sheng Xu <https://orcid.org/0000-0003-0916-3001>;
-  Wenqi Fan <https://orcid.org/0000-0002-5355-5304>;
-  Wangxia Wu <https://orcid.org/0000-0001-5548-8312>;
-  Bing Wang <https://orcid.org/0000-0003-3373-7351>.

Appendix A

In this appendix, to verify the reliability of the CCW theory, the comparison of dimensionless parameters of the cylindrical shock wave, varying with different shock radii, between the CCW theory and numerical simulation is presented in figure 21. Here, V_{ms} and p_s represent the velocity magnitude and pressure at the wavefront of the cylindrical shock wave. Subscript 0 indicates that the cylindrical shock wave radius equals R_0 . It is found that the CCW theory can better predict the convergence of the cylindrical shock wave, although the deviation of the cylindrical shock intensity obtained by the CCW theory and the numerical simulation is observed. Actually, to avoid this deviation (Zhang 2017), we can make the shock intensity at the $R = R_0$ equal to our desired value by constantly adjusting the initial cylindrical shock intensity at R_{int} (R_{int} is much bigger than R_0 in the case of the converged shock wave, and R_{int} is much smaller than R_0 in the case of the diverged shock wave).

Appendix B

In this appendix, the grid independence verification is performed, taking the case of the cylindrical shock wave interacting with a water column. Here, the incident shock wave

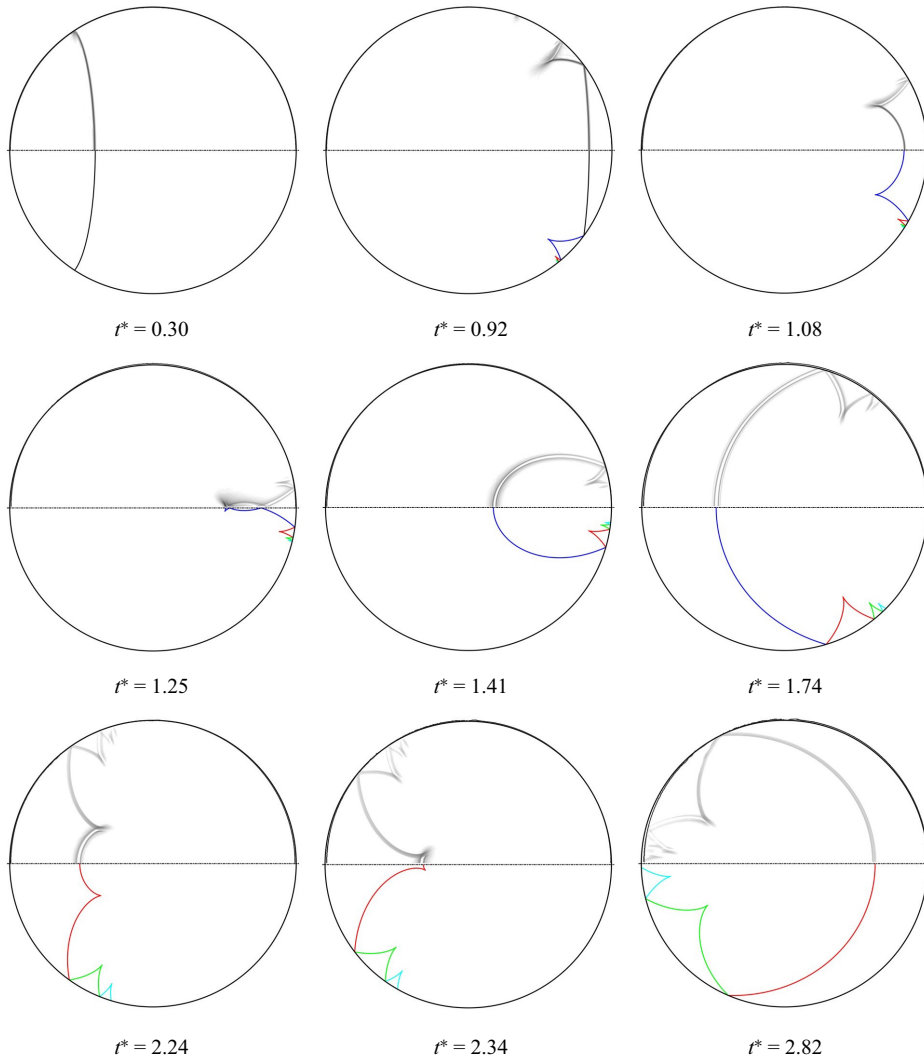


Figure 24. Comparison of the confined wave structure spatio-temporal dynamics theoretically predicted (bottom side) with numerical schlieren contour (top side) for the interaction between the cylindrical converged shock and the water column in the case of $\omega = 4.0$ and $M_0 = 2.4$.

intensity M_0 is taken as 2.4, and the dimensionless incident shock wave radius ω is taken as 4.0. The grid sensitivity is analysed by choosing three different grid resolutions: 5.8 (Grid-I), 13.0 (Grid-II) and 23.0 million cells (Grid-III). The grid cells per the water column diameter correspond to 800, 1200 and 1600, respectively.

The pressure contours and numerical schlieren contours for three different grid resolutions at the same instant are shown in figure 22. A similar distribution is noticed for pressure contours and numerical schlieren contours of the three different grid levels. As the grid resolution is enhanced, the captured flow field structures, including the shock wave structures and two-phase interfaces, become sharper. The extracted pressure profiles along the symmetrical axis of the water column under three different grid resolutions are shown in figure 23, where the abscissa axis is normalised by R_D . The three pressure curves with

different grid resolutions are basically overlapping, and the pressure discontinuity caused by the reflected rarefaction wave is sharpened with the increase of grid resolution. Slight deviations from the pressure distribution are observed behind the reflected rarefaction wave in Grid-I due to the low grid resolution, while the pressure distributions overlap well for the other two higher grid resolutions. Grid-II is finally chosen in the present study to balance the resolution of the flow field and the computational efficiency.

Appendix C

The comparison of wave structure evolution characteristics between the numerical simulation (top side) and the theoretical result (bottom side) for the interaction between the cylindrical converged shock and the water column in the case of $\omega = 4.0$ and $M_0 = 2.4$ is presented in this appendix in [figure 24](#). It is easily found that the theoretical analysis method can perfectly reveal the spatio-temporal evolution of wave structures inside the shocked water column, although small offsets are captured when the shocked water column appears to have a slight deformation.

REFERENCES

- ABGRALL, R. & KARNI, S. 2001 Computations of compressible multifluids. *J. Comput. Phys.* **169** (2), 594–623.
- ALLAIRE, G., CLERC, S. & SAMUEL, K. 2002 A five-equation model for the simulation of interfaces between compressible fluids. *J. Comput. Phys.* **181** (2), 577–616.
- BACH, G.G. & LEE, J.H.S. 1970 An analytical solution for blast waves. *AIAA J.* **8** (2), 271–275.
- BIASIORI-POULANGES, L. & EL-RABII, H. 2019 High-magnification shadowgraphy for the study of drop breakup in a high-speed gas flow. *Opt. Lett.* **44** (23), 5884–5887.
- BIASIORI-POULANGES, L. & EL-RABII, H. 2021 Shock-induced cavitation and wavefront analysis inside a water droplet. *Phys. Fluids* **33** (9), 097104.
- BOYD, B. & JARRAHBASHI, D. 2021 Numerical study of the transcritical shock-droplet interaction. *Phys. Rev. Fluids* **6** (11), 113601.
- BRENNEN, C.E. 2013 *Cavitation and Bubble Dynamics*. Cambridge University Press.
- CHESTER, W. 1954 CXLV. The quasi-cylindrical shock tube. *Lond. Edinb. Dublin Philos. Mag. J. Sci.* **45** (371), 1293–1301.
- CHISNELL, R.F. 1957 The motion of a shock wave in a channel, with applications to cylindrical and spherical shock waves. *J. Fluid Mech.* **2** (3), 286–298.
- CHOUNG, H., SARAVANAN, V., LEE, S. & CHO, H. 2021 Nonlinear weighting process in ghost-cell immersed boundary methods for compressible flow. *J. Comput. Phys.* **433**, 110198.
- FERIL, L.B. & KONDO, T. 2004 Biological effects of low intensity ultrasound: the mechanism involved, and its implications on therapy and on biosafety of ultrasound. *J. Radiat. Res.* **45** (4), 479–489.
- FIELD, J.E., CAMUS, J.-J., TINGUELY, M., OBRESCHKOW, D. & FARHAT, M. 2012 Cavitation in impacted drops and jets and the effect on erosion damage thresholds. *Wear* **290–291**, 154–160.
- FIELD, J.E., DEAR, J.P. & OGREN, J.E. 1989 The effects of target compliance on liquid drop impact. *J. Appl. Phys.* **65** (2), 533–540.
- GOTTLIEB, S. & SHU, C.-W. 1998 Total variation diminishing Runge–Kutta schemes. *Math. Comput.* **67** (221), 73–85.
- GUAN, B., LIU, Y., WEN, C.-Y. & SHEN, H. 2018 Numerical study on liquid droplet internal flow under shock impact. *AIAA J.* **56** (9), 3382–3387.
- HALLER, K.K., POULIKAKOS, D., VENTIKOS, Y. & MONKEWITZ, P. 2003 Shock wave formation in droplet impact on a rigid surface: lateral liquid motion and multiple wave structure in the contact line region. *J. Fluid Mech.* **490**, 1–14.
- HALLER, K.K., VENTIKOS, Y., POULIKAKOS, D. & MONKEWITZ, P. 2002 Computational study of high-speed liquid droplet impact. *J. Appl. Phys.* **92** (5), 2821–2828.
- HEYMANN, F.J. 1969 High-speed impact between a liquid drop and a solid surface. *J. Appl. Phys.* **40** (13), 5113–5122.
- HSIANG, L.-P. & FAETH, G. 1992 Secondary drop breakup in the deformation regime. In *30th Aerospace Sciences Meeting and Exhibit*. American Institute of Aeronautics and Astronautics.

- HSIANG, L.-P. & FAETH, G. 1993 Deformation and secondary breakup of drops. In *31st Aerospace Sciences Meeting*. American Institute of Aeronautics and Astronautics.
- IGRA, D. & SUN, M. 2010 Shock-water column interaction, from initial impact to fragmentation onset. *AIAA J.* **48** (12), 2763–2771.
- IGRA, D. & TAKAYAMA, K. 2001a Investigation of aerodynamic breakup of a cylindrical water droplet. *Atomiz. Sprays* **11** (2), 20.
- IGRA, D. & TAKAYAMA, K. 2001b Numerical simulation of shock wave interaction with a water column. *Shock Waves* **11** (3), 219–228.
- JOHNSEN, E. & COLONIUS, T. 2006 Implementation of WENO schemes in compressible multicomponent flow problems. *J. Comput. Phys.* **219** (2), 715–732.
- JOHNSEN, E. & COLONIUS, T. 2009 Numerical simulations of non-spherical bubble collapse. *J. Fluid Mech.* **629**, 231–262.
- KIM, Y.-S., RHM, H., CHOI, M.J., LIM, H.K. & CHOI, D. 2008 High-intensity focused ultrasound therapy: an overview for radiologists. *Korean J. Radiol.* **9** (4), 291.
- KONDO, T. & ANDO, K. 2016 One-way-coupling simulation of cavitation accompanied by high-speed droplet impact. *Phys. Fluids* **28** (3), 033303.
- LANDGRAF, L., KOZLOWSKI, A., ZHANG, X., FOURNELLE, M., BECKER, F.-J., TRETBAR, S. & MELZER, A. 2022 Focused ultrasound treatment of a spheroid in vitro tumour model. *Cells* **11** (9), 1518.
- LIANG, Y., JIANG, Y., WEN, C.-Y. & LIU, Y. 2020 Interaction of a planar shock wave and a water droplet embedded with a vapour cavity. *J. Fluid Mech.* **885**, R6.
- LOMBARDINI, M., PULLIN, D.I. & MEIRON, D.I. 2014 Turbulent mixing driven by spherical implosions. Part I. Flow description and mixing-layer growth. *J. Fluid Mech.* **748**, 85–112.
- LUKKA, H., WALDRON, T., CHIN, J., MAYHEW, L., WARDE, P., WINQUIST, E., RODRIGUES, G. & SHAYEGAN, B. 2010 High-intensity focused ultrasound for prostate cancer: a practice guideline. *Can. Urol. Assoc. J.* **4** (4), 232–236.
- MALIK, V., HYTOVICK, R., CHIN, H.M., BURKE, R.F., REZZAG, T., STIEHL, B., MORALES, A. & AHMED, K.A. 2022 Exploration of RP-2 liquid droplets interaction with a detonation wave. In *AIAA SCITECH 2022 Forum*. American Institute of Aeronautics and Astronautics.
- MENG, J.C. & COLONIUS, T. 2015 Numerical simulations of the early stages of high-speed droplet breakup. *Shock Waves* **25** (4), 399–414.
- MENG, J.C. & COLONIUS, T. 2018 Numerical simulation of the aerobreakup of a water droplet. *J. Fluid Mech.* **835**, 1108–1135.
- MITTELSTEIN, D.R., YE, J., SCHIBBER, E.F., ROYCHOUDHURY, A., MARTINEZ, L.T., FEKRAZAD, M.H., ORTIZ, M., LEE, P.P., SHAPIRO, M.G. & GHARIB, M. 2020 Selective ablation of cancer cells with low intensity pulsed ultrasound. *Appl. Phys. Lett.* **116** (1), 013701.
- NAGAYAMA, K., MORI, Y., MOTEGI, Y. & NAKAHARA, M. 2006 Shock hignoniot for biological materials. *Shock Waves* **15** (3), 267–275.
- OBRESCHKOW, D., DORSAZ, N., KOBEL, P., DE BOSSET, A., TINGUELY, M., FIELD, J. & FARHAT, M. 2011 Confined shocks inside isolated liquid volumes: a new path of erosion?. *Phys. Fluids* **23** (10), 101702.
- PILCH, M. & ERDMAN, C.A. 1987 Use of breakup time data and velocity history data to predict the maximum size of stable fragments for acceleration-induced breakup of a liquid drop. *Intl J. Multiphase Flow* **13** (6), 741–757.
- SARAVANAN, V., CHOUNG, H. & LEE, S. 2021 Cell-based hybrid adaptive mesh refinement algorithm for immersed boundary method. *Intl J. Numer. Methods Fluids* **94** (3), 272–294.
- SAUREL, R., PETITPAS, F. & ABGRALL, R. 2008 Modelling phase transition in metastable liquids: application to cavitating and flashing flows. *J. Fluid Mech.* **607**, 313–350.
- SEMBIAN, S., LIVERTS, M., TILLMARK, N. & APAZIDIS, N. 2016 Plane shock wave interaction with a cylindrical water column. *Phys. Fluids* **28** (5), 056102.
- SHARMA, S., PRATAP SINGH, A., SRINIVAS RAO, S., KUMAR, A. & BASU, S. 2021 Shock induced aerobreakup of a droplet. *J. Fluid Mech.* **929**, A27.
- THEOFANOUS, T.G. & LI, G.J. 2008 On the physics of aerobreakup. *Phys. Fluids* **20** (5), 052103.
- THEOFANOUS, T.G., LI, G.J. & DINH, T.N. 2004 Aerobreakup in rarefied supersonic gas flows. *Trans. ASME J. Fluids Engng* **126** (4), 516–527.
- THOMPSON, K.W. 1987 Time dependent boundary conditions for hyperbolic systems. *J. Comput. Phys.* **68** (1), 1–24.
- THOMPSON, K.W. 1990 Time-dependent boundary conditions for hyperbolic systems, II. *J. Comput. Phys.* **89** (2), 439–461.
- TITAREV, V.A. & TORO, E.F. 2004 Finite-volume WENO schemes for three-dimensional conservation laws. *J. Comput. Phys.* **201** (1), 238–260.

Curved shock interaction with water column

- TORO, E. 2009 Riemann solvers and numerical methods for fluid dynamics: a practical introduction. In *Riemann Solvers and Numerical Methods for Fluid Dynamics*. Springer.
- WANG, B., XIANG, G. & HU, X.Y. 2018 An incremental-stencil WENO reconstruction for simulation of compressible two-phase flows. *Intl J. Multiphase Flow* **104**, 20–31.
- WHITHAM, G.B. 1957 A new approach to problems of shock dynamics. Part I. Two-dimensional problems. *J. Fluid Mech.* **2** (2), 145–171.
- WHITHAM, G.B. 1958 On the propagation of shock waves through regions of non-uniform area or flow. *J. Fluid Mech.* **4** (4), 337.
- WHITHAM, G.B. 1959 A new approach to problems of shock dynamics. Part 2. Three-dimensional problems. *J. Fluid Mech.* **5** (3), 369–386.
- WU, J., LIU, H. & XIAO, Z. 2021a Refined modelling of the single-mode cylindrical Richtmyer–Meshkov instability. *J. Fluid Mech.* **908**, A9.
- WU, W., LIU, Q. & WANG, B. 2021b Curved surface effect on high-speed droplet impingement. *J. Fluid Mech.* **909**, A7.
- WU, W., XIANG, G. & WANG, B. 2018 On high-speed impingement of cylindrical droplets upon solid wall considering cavitation effects. *J. Fluid Mech.* **857**, 851–877.
- XIANG, G. & WANG, B. 2017 Numerical study of a planar shock interacting with a cylindrical water column embedded with an air cavity. *J. Fluid Mech.* **825**, 825–852.
- ZHAI, Z., LIU, C., QIN, F., YANG, J. & LUO, X. 2010 Generation of cylindrical converging shock waves based on shock dynamics theory. *Phys. Fluids* **22** (4), 041701.
- ZHAI, Z.G., ZHANG, F., ZHOU, Z.B., DING, J.C. & WEN, C.-Y. 2019 Numerical study on Rayleigh–Taylor effect on cylindrically converging Richtmyer–Meshkov instability. *Sci. China Phys. Mech. Astron.* **62** (12), 124712.
- ZHANG, F. 2017 Dynamic characteristic of converged shock wave and its induced interfacial instability (in Chinese). Doctoral dissertation, University of Science and Technology of China.